2005

Preparation of SERS substrate using self-assembled nanoporous polymer

Kazi Asma Sultana
San Jose State University

NOTE TO USERS

PREPARATION OF SERS SUBSTRATE USING SELF-ASSEMBLED NANOPOROUS POLYMER

A Thesis

Presented to

The Faculty of the Department of Chemical and Materials Engineering

San Jose State University

In Partial Fulfillment

of the Requirements for the Degree

Master of Science

By

Kazi Asma Sultana

December 2005

APPROVED FOR THE

DEPARTMENT OF CHEMICAL AND MATERIALS ENGINEERING

Stacy H Gl

Dr. Stacy Gleixner

Karamjeet Arya

Dr. Karamjeet Arya

Danielle R. Chamberlin

Dr. Danielle Chamberlin, Agilent Technologies Laboratories

APPROVED FOR SAN JOSE STATE UNIVERSITY

Rhea L. Williamson 12/12/05

ABSTRACT

PREPARATION OF SERS SUBSTRATE USING SELF-ASSEMBLED NANOPOROUS POLYMER

By Kazi A. Sultana

SERS (Surface Enhanced Raman Spectroscopy) is a spectroscopic technique. Weak Raman signal is enhanced many folds using noble metal nanoparticles or a roughened noble metal surface. Thus SERS is an improvement on Raman spectroscopy providing enough sensitivity for the tool to detect a single molecule. The widespread use of SERS is hindered due to the lack of highly reproducible substrates.

In this research, silver nanoparticles were prepared using templating technique. The use of PS-PFEMS diblock copolymer as a template to prepare silver nanoparticles for SERS was investigated. Nanoislands of silver were prepared on silicon covered with thermal oxide using the polymer template. λ-DNA was also used as a template to synthesize silver nanoparticles on mica. The effectiveness of these samples for SERS was determined using nicotine. The characteristic peak of nicotine around 1030 cm^{-1} was obtained with these samples for 1 ppt nicotine solution.

ACKNOWLEDGMENTS

The author wishes to thank Dr. Stacy Gleixner, Dr. Karamjeet Arya, and Dr. Danielle Chamberlin for their time and expert advice. Since this research was done at Agilent Technologies Laboratories, the author would like to thank the many individuals for their time and resources. The SJSU foundation is acknowledged for collaborating with the Agilent research grant.

For the thermal oxide deposition and E-beam evaporation work, the author acknowledges Dr. Qing Bai and Young Yim. For SEM measurements, the author thanks Grant Girolami. Dr. Maozi Liu and Jennifer Lu are acknowledged for the polymer and the λ-DNA part of the research. Dr. Karen Seaward is acknowledged for her assistance in performing the contact angle measurements.

TABLE OF CONTENTS

LIST OF FIGURES

LIST OF TABLES

CHAPTER 1

INTRODUCTION

Surface Enhanced Raman Spectroscopy (SERS) is an ideal tool for trace chemical and biological analysis as well as for in-situ investigations of various interfacial processes [1]. SERS is an improvement on Raman spectroscopy due to the unique optical properties of noble metal nanoparticles [1]. It can provide a fingerprint of almost any organic substances with high sensitivity. It can give information on surface and interface processes. SERS is promising in the fields of biophysics and lifescience [2]. It has in-situ analysis capability. The technique is fast with great sensitivity which allows the monitoring of real time reactions. Sample contact with the tool is not required. It is a non-destructive analytical technique and suitable for analysis in biological and biophysical environments. Detection of single molecule with SERS has been reported with the enhancement factor on the order of 10^{20} [3]. A widely used analytical technique in these fields is fluorescence spectroscopy to detect a single molecule, but often photobleaching limits the number of photons obtainable from a single molecule [3]. So SERS may be an alternative to fluorescence spectroscopy. Single molecule detection makes SERS promising in applications that require ultrasensitive and multiplexing detection of biomolecules and in non-invasive in -vivo medical treatment [4].

Raman spectroscopy is a vibrational characterization technique. It is based on the inelastic light scattering phenomenon. When a photon with a certain energy inelastically collides with a molecule, it's energy changes due to the vibrational energy of the

molecule. Since the vibrational energy of a molecule depends on the bond strength, types of bond and it's surrounding environment, Raman spectroscopy gives a fingerprint of a molecule [3]. The limitations of Raman spectroscopy is that not many photons are shifted by the vibrational energy of molecule. One out of 10^{11} photons has a vibrational energy shift [3]. Due to the inefficiency of the Raman scattering process, a Raman signal is really weak. A lot of researches has been done to overcome it's inherent weakness of sensitivity. No significant improvements were found in this field until Fleischmann *et al.* observed the intense Raman spectra of pyridine adsorbed on a silver electrode in 1974 [4]. The enhancement factor was estimated at approximately 10^5 to 10^6 times that which would be expected for pyridine in solution [4]. This observation promoted the extensive investigation of the phenomenon which is known as Surface Enhanced Raman scattering [4].

The enhancement mechanism of Surface Enhanced Raman Spectroscopy (SERS) is based on the unique optical properties of metal nanoparticles. When the target molecules come close to noble metal nanoparticles, they experience a larger electric field and the Raman scattering process becomes much more probable. As a result, Raman signals are strongly increased. Localized Surface Plasmon Resonance (LSPR) of noble metal nanoparticles plays a key role in enhancement of the Raman signal.

Localized Surface Plasmon Resonance (LSPR) is a unique optical characteristic of noble metal nanoparticles [5]. When an incident radiation of a certain frequency interacts with the surface of a nanoparticle, it creates plasmons [5]. Plasmons are

collective excitations of conduction electrons. Plasmons create strong electric dipoles in the metal nanoparticles. The strength of Raman scattering is proportional to four times this local electric field [5]. The enhancement of the Raman signals take place in the local electric fields of metallic nanoparticles [5]. When the target analyte is placed on the surface of the metal nanoparticles in the strong electric field, the strength of Raman scattering can therefore be increased by many orders of magnitude.

The resonance frequency of the localized surface plasmons depends on the size, shape, and external dielectric environment of the nanoparticles [5]. When plasmons are in resonance with the incident wavelength of light, enhancement increases greatly. It is observed that in an aggregates of noble metal nanoparticles, a very small number of nanoparticles exhibit high enhancement efficiencies. Only the surface plasmons of those particles get coupled with incident light and emit bright light. They are called "hot particles." To prepare a SERS active substrate with all the particles "hot" in a reproducible manner is an engineering challenge.

One of the main obstacles for widespread application of SERS for routine chemical and biological analysis is the difficulties in obtaining reproducible SERS-active substrate. Standard nanofabrication techniques to prepare nanoparticle structures are Electron Beam Lithography (EBL), Ion Beam Lithography (IBL), and X-ray Lithography (XRL) [5]. They have inherent features that limit their applicability [5]. The bottom-up approaches using self-assembled nanoporous material as a template is an interesting route to produce periodic particle array of silver with small particle size and small spacing.

Diblock copolymers are an ideal material for this respect. Since in a diblock copolymer two chemically distinct chains are connected to each other, the molecules self-assemble into ordered morphologies with a size scale limited to molecular dimension [6]. Block copolymers which self assemble into cylindrical microdomains of the minor component are used as a template. Then the selective etching of the one of the components of the diblock copolymer film will result in an array of nanopores.

A template for a periodic array can also be made with DNA. DNA molecules self-assemble into a nanoporous material because of their inherent long chain structure and large aspect ratio (length: diameter). Moreover, self-assembly of DNA is highly parallel and inherently fast [6].

In this research project, Poly Styrene-Poly Ferrocenyl Ethyl Methyl Silane (PS-PFEMS) diblock copolymer and λ-DNA were used as templates. Silver nanoislands on silicon with thermal oxide were formed using PS-PFEMS as a template. Scanning Electron Microscope (SEM) was used for structural characterization. Control over the size of the nanoparticles was poor. There are difficulties in polymer deposition on silicon to get uniformity in the periodicity of the cylindrical microdomains of PFEMS in PS matrix. Silver nanoparticles were also synthesized using a λ- DNA (48500 base pairs) network as a template on a mica substrate. Silver ions were first selectively adsorbed on the DNA network and then reduced in sodium borohydride solution to form silver particles. The diameter of the silver nanoparticles can be controlled by adjusting the concentration of the DNA solution and the reducing time. Structural characterization of

the periodic particle arrays of Ag was done with an Atomic Force Microscopy (AFM). SERS (Surface Enhanced Raman Spectroscopy) was used as a diagnostic tool to determine the effectiveness of the sample as SERS-active substrate. It showed an enhanced Raman signal comparable to substrates prepared by a standard method such as electron beam lithography.

The outline of this thesis is as follows. Since the optical properties of metal nanoparticles have a primary role in SERS, they are first discussed in Chapter 2. Basic theory of Raman scattering and the enhancement mechanisms of SERS are also discussed in this chapter. In Chapter 3, the most commonly used SERS substrate preparation techniques are overviewed. In Chapter 4, the experimental procedures used in this research are discussed. This includes the fabrication schemes using a self-assembled nanoporous polymer PS-PFEMS and λ-DNA as templates. In Chapter 5, results and discussions are presented followed by summary in Chapter 6.

CHAPTER 2

BACKGROUND

2.1 Raman Spectroscopy

Raman Spectroscopy, a useful analytical technique for chemical and biological analysis, is based on the Raman effect. The Raman effect is inelastic scattering of light by molecules. Thus Raman scattering is the change in frequency for a small percentage of intensity in a monochromatic beam due to the interaction with some material.

When an incident photon of frequency ν_0 (energy $h\nu_0$) interacts with the molecules having vibrational energy levels of ν_1, ν_2, two types of collisions happen: (i) elastic and (ii) inelastic. Most of the collisions are elastic where energy of the scattered photons does not change. But due to some inelastic collisions, energy of some scattered photons is lower or higher than the incident photon. Raman spectroscopy is the measurement of the wavelength and intensity of inelastically scattered light from molecules [7]. The Raman scattered light occurs at wavelengths that are shifted from the incident light by the energies of molecular vibrations. Figure1 illustrates Raman shift in a simple schematic diagram.

The experimental problems of Raman spectroscopy are the low intensity of the inelastic scattering and the much larger intensity of the elastic scattering. This causes the cross section of Raman process to be 12-14 orders of magnitude below typical

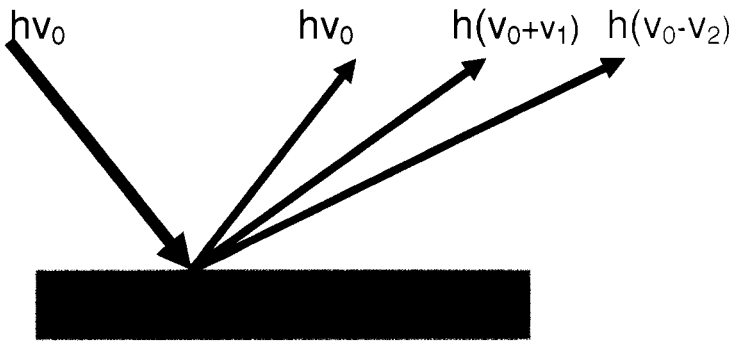

Figure 1. Schematic diagram showing different types of photon scattering in Raman process.

fluorescence cross sections. Normal Raman Spectroscopy is ineffective for surface studies because the photons of the incident laser light simply propagate through the bulk and the signal from the bulk overwhelms any Raman signal from the analytes at the surface.

2.2 Surface Enhanced Raman Spectroscopy

Surface Enhanced Raman Spectroscopy (SERS) is a Raman Spectroscopy (RS) technique that provides greatly enhanced Raman signal from Raman-active analyte molecules that have been adsorbed onto certain specially prepared metal surfaces [3]. The enormous enhancement of Raman intensity for molecules adsorbed on rough surfaces was first observed in 1974 [8]. The highest reported Raman enhancement factor is 10^{14} [3].

Theoretical models of SERS generally involve two major types of enhancement mechanisms: (1) electromagnetic effect or field effect and (2) chemical effect. The classical theory of light scattering is helpful to understand the basics of the enhancement effects of SERS. An incident light beam induces a dipole moment in a particle which scatters light at the frequency of the dipole moment which can be represented by Equation 1, where ν is the dipole scattering frequency and μ^0 is the maximum induced dipole moment for a given frequency component of μ [7].

$$\mu(t) = \mu^0 \cos(2\pi\nu t) \qquad \text{Equation 1}$$

If the incident electric field E_{inc} is not too large, the induced dipole moment can be approximated as Equation 2 where P is the polarizability of the molecules. Raman intensity is proportional to the square of the induced dipole μ [7].

$$\mu(t) = P.E_{inc}(t) \qquad \text{Equation 2}$$

From Equation 2 it can be seen that there are two possible enhancement mechanisms to enhance either (i) the polarizability or (ii) the electric field. An electromagnetic enhancement of the Raman signal is known as the 'electromagnetic effect' or 'field effect' in which the target molecule experiences large local fields caused by electromagnetic resonance occurring near metal surfaces [9]. Chemical enhancement, also known as the 'molecular effect', can be achieved by increasing the molecular polarizability. The interaction of the metal surface and molecules changes the

polarizability of the target molecules. The "Chemical effect" or chemical enhancement on the Raman spectra is relatively small [10].

A SERS-active substrate typically consists of noble metal nanoparticles which have an unique property of electromagnetic resonance called surface plasmons. When excited by the incident radiation at the plasmon resonance frequency, the rough metal surface or metal nanostructures induce large local fields on the surface. These enhanced local fields contribute to the electromagnetic enhancement of Raman signal by many orders of magnitude. In the following section the properties of surface plasmons are discussed to better understand their contribution to SERS before returning to the details of SERS mechanism.

2.3 Surface Plasmon and Optical Properties of Noble Metal Nanoparticle

Plasma oscillation is the collective oscillation of electrons in a metal whose conduction electrons move freely. A metal consists of two parts: (i) the positive ions which make the regular lattice and (ii) the surrounding conduction electrons which can move freely. The negative electronic charge is balanced by the positive charge of the ionized metal atoms in equilibrium. In a simple model, electrons behave like a gas whose density can fluctuate by external excitations. If the balance is somehow disturbed by increasing the electron density in a local region, the region becomes negatively charged. Because of the electron-electron coulomb repulsion, the electrons will move away from the region. However, because of inertia, the electrons will keep on moving away from the region even after the system becomes neutral. This will make the region positively

charged after some time. The electrons will then be attracted to this region again and will eventually overshoot the equilibrium situation to accumulate and make it negatively charged. The whole cycle will repeat itself until the energy that caused the initial disturbance is dissipated [8]. Thus an oscillation of free electron in metals can be induced which is called plasma oscillation. A plasmon is a quantum of plasma oscillation. In a bulk metal, charge density oscillates at the plasma frequency. Equation 3 provides the expression for plasma frequency where N is the density of electrons, e is the electric charge and m is the mass of the electron.

$$\omega_p = \sqrt{\frac{4\pi N e^2}{m\varepsilon_0}} \qquad \text{Equation 3}$$

Charge density or electron plasma oscillation at a metal surface is known as surface plasmon (SP). For a flat metal surface, the mobility of an electron in a plane parallel to surface is very high compared to the mobility in the direction perpendicular to surface. Thus surface plasmons are basically a longitudinal charge density oscillation. Figure 2 shows a schematic drawing of SP, propagating as a polarization wave at the metal-dielectric/vacuum/air boundary.

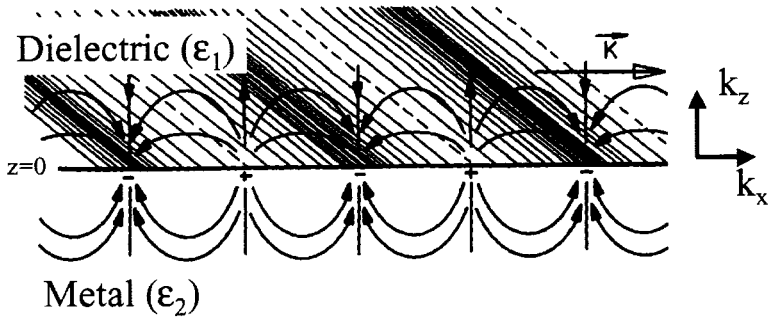

Figure 2. Field configuration of surface plasmon bound at the interface between a metal and dielectric [7].

The wave vector for the surface plasmon is expressed by Equation 4, where the wave vector of light in free space, $k_0 = \frac{\omega}{c}$, ε_1 is the dielectric function of metal, and ε_2 is the dielectric function of medium.

$$K_{SP} = K_0 \sqrt{\frac{4\varepsilon_1 \varepsilon_2}{\varepsilon_1 + \varepsilon_2}} \qquad \text{Equation 4}$$

For a metal surface in vacuum or air, $\varepsilon_2 = 1$ and $\varepsilon_1 < 0$. Thus the surface plasmon will always have a longer wave vector than the light waves of same energy. So freely propagating light will not be able to excite surface plasmon because energy and momentum cannot be conserved at the same time. The wave vector mismatch is seen in the dispersion curve, which is shown in Figure 3.

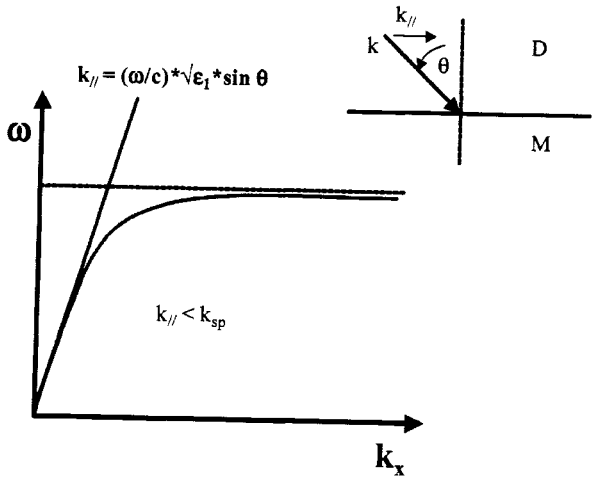

Figure 3. Dispersion relation to surface plasmon with light [4].

For a given frequency, ω, the component of the wave vector of light, travelling in the dielectric/air/vacuum in the plane of the surface will be shown in Equation 5.

$$k_{surface} = \frac{\omega}{c} * \sqrt{\varepsilon_1} * \sin\theta \qquad \text{Equation 5}$$

As shown in Figure 3, this line is always to the left of the SP curve, hence unable to excite a SP.

2.4 Localized Surface Plasmon

For metal nanoparticles, electrons can be collectively excited at the inside of the nanoparticle. As a result, a localized surface plasmon will be formed. If the particle dimension is smaller than the wavelength of incident light, a localized surface plasmon can be modelled as an induced electric dipole. Figure 4 shows the diploes induced in

nanoparticles. The displacement of conduction electron charges relative to the nuclei creates the dipoles.

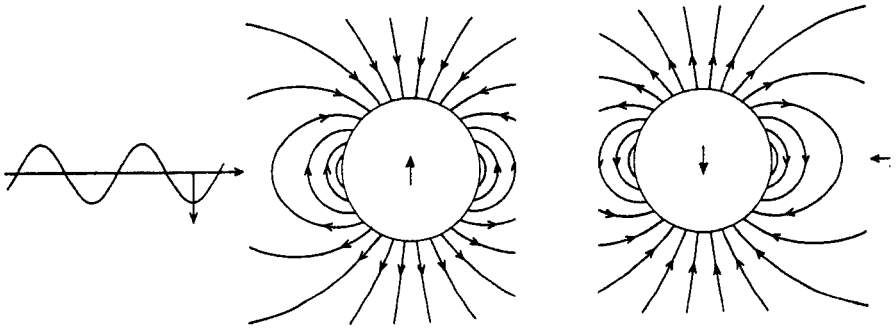

Figure 4. Schematic illustration of the dipolar plasmon in nanosphere [8].

For very small nanoparticles the magnitude of the induced electric field inside the particle is expressed by Equation 6, where ε_1 is the complex dielectric function of metal and ε_2 is the dielectric function of surrounding material.

$$E_0 = 4\pi a^3 \frac{\varepsilon_1 - \varepsilon_2}{\varepsilon_1 + 2\varepsilon_2} E_0 \qquad \text{Equation 6}$$

The condition for maximum induced electric field due to localized surface plasmon resonance (LSPR) is expressed in Equation 7.

$$\mathrm{Re}(\varepsilon_1) = -2\,\varepsilon_2 \text{ and } \mathrm{Im}(\varepsilon_1) = 0 \qquad \text{Equation 7}$$

Thus the choice of metal for the nanoparticle is important. The frequency dependent dielectric function of the metal can be written as Equation 8, where γ is the damping

coefficient introduced to allow for the loss of the electromagnetic energy within the metal and ω_p is the plasmon frequency as defined in Equation 3.

$$\varepsilon_1 = 1 - \frac{\omega_p^{\ 2}}{\omega^2 - i\omega\gamma} \qquad \text{Equation 8}$$

Figure 5 shows the experimental dielectric function of gold and silver for different frequencies. From Figure 5, it is seen that at the visible region, gold and silver satisfies both the conditions of Equation 7. This is why in the visible region SERS phenomenon occurs most efficiently for gold or silver nanoparticles.

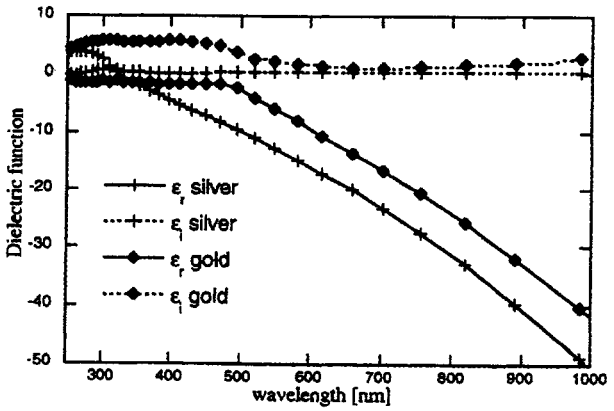

Figure 5. Experimental data of dielectric function of silver and gold [7].

The simple model of Equation 6 shows that the enhanced electric field due to nanoparticle is dependent on the nanoparticle material, nanoparticle radius, dielectric constant, and the environment.

2.5 SERS Enhancement Mechanisms

As discussed in Section 2.1, when an incident photon with $h\upsilon_0$ energy interacts with a molecule, an elastic collision occurs. It is called Rayleigh scattering for which energy of the incident photon will not change. In inelastic scattering the energy of incident photon changes due to the molecular vibrational energy of the target molecule ($h\upsilon_M$). In inelastic scattering, two types of phenomenon can occur: (i) Stokes and (ii) Anti-stokes. In Stokes scattering, the scattered photon has lower energy than that of incident photon. On the other hand, due to Anti-stokes scattering, the scattered photon leaves with a higher energy than the incident photon. Concepts of Raman Scattering are shown in Figure 6.

In normal Raman scattering, the total Stokes Raman signal $P^{RS}(\upsilon_S)$ is proportional to the Raman cross section $\sigma^R{}_{free}$, the excitation laser intensity $I(\upsilon_L)$ and the number of the probed volume N which is expressed in Equation 9.

$$P^{RS}(\upsilon_S) = N\sigma^R{}_{free} I(\upsilon_L) \qquad \text{Equation 9}$$

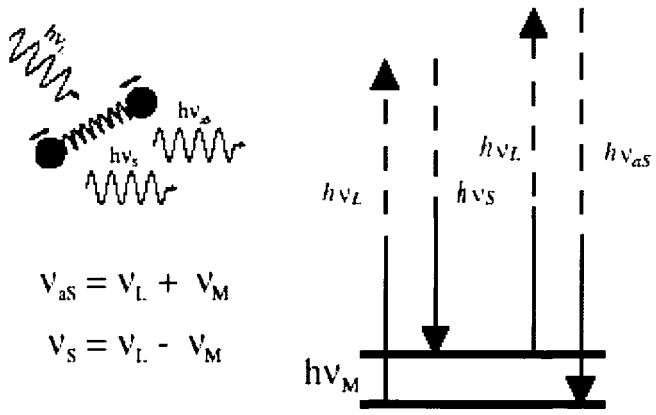

Figure 6. Schematic diagram showing Raman scattering [2].

In SERS, the total power signal is increased due to the specific effects of metal nanoparticles which can be expressed by Equation 10, where N' is the number of molecules involved in SERS process, σ^{R}_{ads} is the increased cross section of the new Raman process due to the adsorbed molecule, $|A(\upsilon_L)|$ and $|A(\upsilon_S)|$ are enhancement factor for laser and Raman scattered field.

$$P^{SERS}(\upsilon_S) = N'\sigma^{R}_{ads} I(\upsilon_L)|A(\upsilon_L)|^2 |A(\upsilon_S)|^2 \qquad \text{Equation 10}$$

The schematic diagram to explain the concept of the enhancement factor in SERS due to LSPR is shown in Figure 7, where a nanoparticle with a complex dielectric constant ε is surrounded by a medium of dielectric constant ε_0. The diameter of the particle is less than the wavelength of light. A molecule in the vicinity of the nanosphere with a distance d is exposed to the field E_M

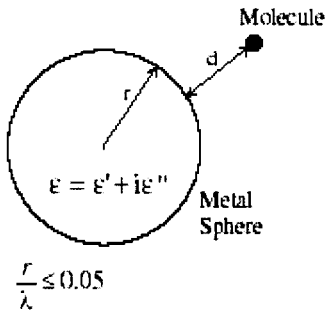

Figure 7. Schematic diagram for understanding the concept of electromagnetic enhancement mechanisms [2].

E_M is the superposition of the incoming field E_0 and the field of dipole E_{sp} which is shown in Equation 11 and Equation 12.

$$E_M = E_0 + E_{SP} \qquad \text{Equation 11}$$

$$E_{SP} = r^3 \frac{\varepsilon - \varepsilon_0}{\varepsilon + 2\varepsilon_0} E_0 \frac{1}{(r+d)^3} \qquad \text{Equation 12}$$

The field enhancement factor is defined as the ratio of the electromagnetic field experienced by the target analyte particle to that of the incident light which is shown in Equation 13 [6].

$$A(\upsilon) = \frac{E_M}{E_0} \qquad \text{Equation 13}$$

$$= 1 + \frac{r^3}{(r+d)^3} \frac{\varepsilon - \varepsilon_0}{\varepsilon + 2\varepsilon_0}$$

$$\approx \frac{r^3}{(r+d)^3}\frac{\varepsilon-\varepsilon_0}{\varepsilon+2\varepsilon_0}$$

Raman scattering intensity is the square of far-field amplitude of E_M. Equation 14 shows the relationship of Raman intensity I_R with field intensity and distance of target molecule.

$$I_R = \lim_{kr\to\alpha} |E_R(d,\omega)\exp(ikd)/d|^2 \qquad \text{Equation 14}$$

The exponential quantity in Equation 14 shows the space dependence of the intensity. An enhancement factor G_{EM} is defined as in Equation 15, where I_R^0 is the Raman intensity in the absence of the metal sphere.

$$G_{EM} = \frac{I_R}{I_R^0} \qquad \text{Equation 15}$$

The laser field as well as the Stokes or anti-Stokes field will be enhanced because of the LSPR if the excitation frequency matches the plasmon resonance frequency. Taking into account enhancing effects for the laser and the Stokes field, the electromagnetic enhancement factor for the Stokes signal power G(vs) can be defined as in Equation 16.

$$G(vs) = |A(\upsilon_L)|^2 |A(\upsilon_S)|^2 \qquad \text{Equation 16}$$

From Equation 16, it can be concluded that the enhancement scales as the fourth power of the local field of the metal nanostructure. Excitation is particularly strong when excitation is on resonance with surface plasmons. Also Equation 16 shows that the

enhancement strongly decreases over distance. Although the target molecules and metal nanostructures need not be in contact, the reduction of enhancement is proportional to $1/d^{12}$.

CHAPTER 3

LITERATURE REVIEW

The goal of this project is to prepare a SERS active substrate. Nanoporous materials are used as template to prepare periodic array of noble metal nanoparticle. Also, silver coated nanosphere glass substrates are being investigated in this work to provide a comparison to the novel materials being developed. Research work related to the various types of SERS substrate preparation and their properties are reviewed in this chapter. Diblock copolymer and λ- DNA are the examples of nanoporous material. Results from different research work on template processing using these materials are discussed.

3.1 SERS Substrate

Different kinds of noble metal nanostructures, such as metal deposited on nanosphere, periodic particle arrays of noble metal, are used as SERS substrates. Nanosphere Lithography (NSL) and Electron Beam Lithography (EBL) are some of the well known techniques to produce periodic nanoparticle array [11]. Aggregates of nanoparticles are used for SERS. Nanoporous materials such as diblock copolymer and DNA can also be used as templates for nanoparticle fabrication [12, 13]. Process steps to prepare different types of SERS substrates and their properties are discussed in the following sections.

3.1.1 Metal Thin Film over Nanospheres

This type of substrate is prepared by forming a spin-coated nanosphere layer on a base, typically glass. The nanospheres are then coated with a metal thin film. R. L. Moody *et al.* prepared latex polystyrene nanospheres on glass microscope slides by spin coating at 800-1200 rpm [14]. Silver was deposited over the nanospheres by using a vacuum evaporator. They conducted experiments to see the effects of the sphere dimension and silver film thickness on SERS.

R. L. Moody *et al.* investigated the effects of parameters such as sphere size, film thickness, and excitation wavelength on SERS intensity. They varied the sphere size ranging from 38 nm to 500 nm, keeping the other parameters fixed. The effect of the sphere diameter on the Raman intensity is shown in Figure 8.

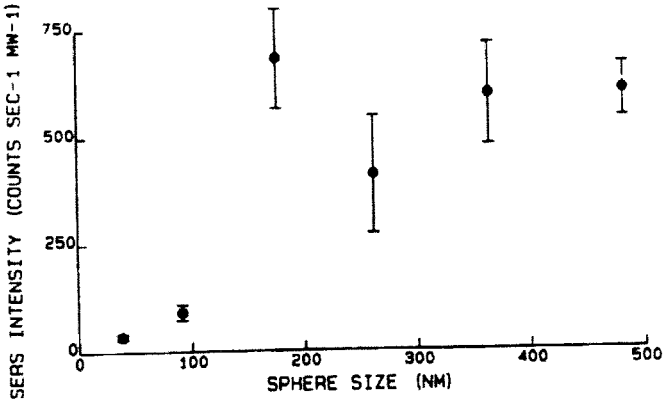

Figure 8. Plot of SERS intensity vs. sphere size [14].

The results show that the SERS intensity for 91 nm and 38 nm diameter spheres is less by a factor of twenty than that for 176 nm diameter. SERS intensity for 261 nm, 364 nm, and 482 nm spheres are similar to that of 176 nm spheres. A SERS reference signal of 1240 cm-1 vibration of 1 nitropyrene was used.

Li Bao *et al.* used silica beads on glass as the nanospheres [15]. Silver was used as the metal thin film coating. They varied silica bead diameter from 100 nm to 800 nm keeping the silver thickness the same. A 1003 cm^{-1} peak of benzoic acid was used as a reference. Figure 9 shows the relative SERS response as a function of silica bead diameter. The results show a linear increase in SERS intensity with diameter up to 565 nm. After 565 nm, the SERS intensity reduces with increasing sphere diameter.

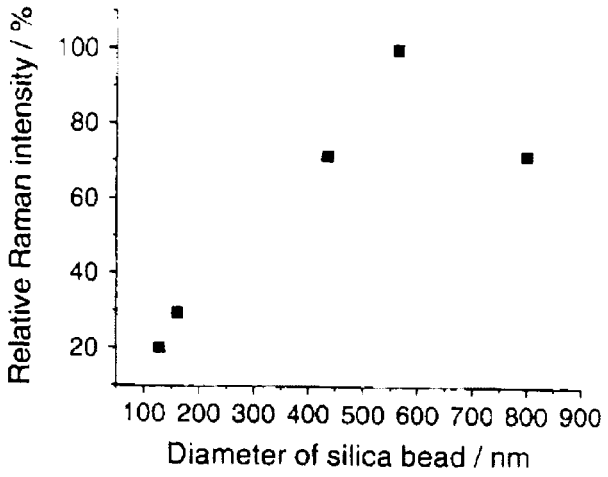

Figure 9. The effect of diameter of silica bead on SERS response [15].

SERS intensity also depends on metal film thickness. To investigate the effects of silver thickness, R. L. Moody *et al.* used glass slides coated with 364 nm polystyrene sphere as samples [14]. The silver thickness over the nanospheres was varied from 25 nm to 125 nm. SERS intensity for silver thicknesses in the range of 50 nm to 100 nm was six times larger than the weakest SERS signal. The ratio of sphere core radius to particle (core and the silver coat) radius is also a measure of film thickness. Figure 10 shows that the maximum SERS intensity was obtained for a ratio of 0.65 to 0.75. Li Bao *et al.* also observed similar maxima in SERS intensity when they varied the silver deposition time [15]. The result is shown in Figure 11.

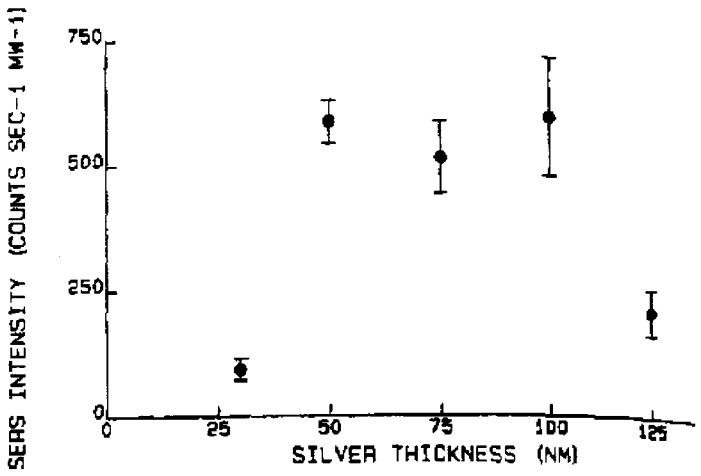

Figure 10. The effects of silver thickness on SERS intensity [14].

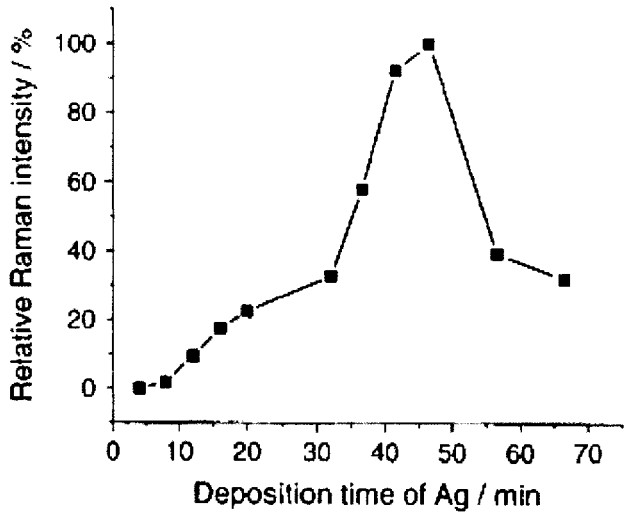

Figure 11. Effect of deposition time on SERS intensity [15].

With an increase of deposition time, Raman intensity increases up to 47 minutes. After that, Raman intensity decreases with increasing deposition time. A sample with a 47 minute deposition time produced film that showed the maximum SERS response. SEM images were taken to explore the morphology of the deposited silver. At short deposition time small number of silver islands having diameter with a few nanometer appeared. With the increase of deposition time, the number of silver islands increased. At larger deposition time the silver islands merged to larger islands in the size range of tens of nanometers. There is range of sizes of the islands for which SERS enhancement got optimized.

The intensity of the SERS signal depends on the excitation wavelength. R. L. Moody *et al.* measured SERS signals for a glass slide sample, coated with 364 nm

diameter spheres and silver, at nine different excitation frequencies [14]. A SERS reference signal of 1240 cm^{-1} vibration of 1 nitropyrene was used. It was found that an excitation at 514.5 nm produces a Raman signal which is 200 times larger than the weakest detected signal. There is an optimal range for the excitation wavelength for which the maximum SERS intensity can be produced.

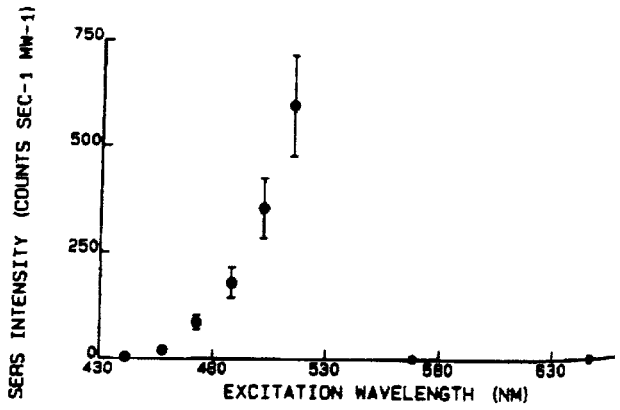

Figure 12. Effects of excitation wavelength on SERS intensity [14].

To get a maximum SERS signal several experimental parameters can be optimized. SERS signals increase significantly with proper choice of sphere size, silver thickness, and the excitation wavelength.

3.1.2 Single-Layer Periodic Particle Array

Nanosphere Lithography (NSL) is a technique that is used to produce periodic particle array structures having nanometer scale features [16]. In NSL, nanospheres are deposited on a substrate. They self-assemble into hexagonally-close packed structures which are used as a deposition mask for the nanoparticles [16]. The size and shape of the nanoparticles depend on the nanosphere diameter and mass thickness which can be predicted from the geometrical models [17]. The projection of holes created by the single layer nanosphere mask is shown in Figure 13, where the inset shows a comparison of the predicted geometry by the gray area to that of the actual projection of the hole created by the nanosphere mask by black area [17].

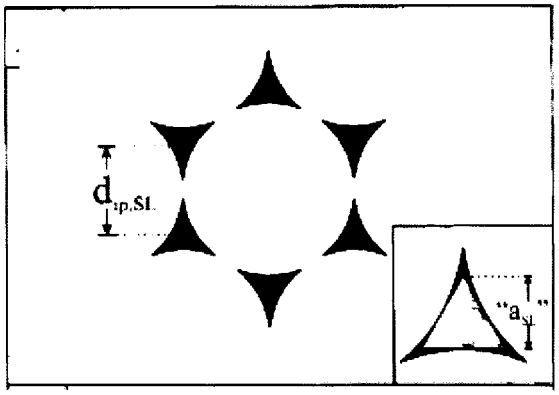

Figure 13. Projection of holes created by a single layer nanosphere mask [17].

According to the geometric model, the predicted particle geometry for a single layer mask is the largest inscribed equilateral triangle. From geometry, the predicted interparticle spacing is related to the diameter of the nanosphere by Equation 17, where d_{ip} is the interparticle spacing, D the nanosphere diameter, and *a* the in-plane width of nanoparticle [17].

$$d^{geom}_{ip,SL} = \frac{D}{\sqrt{3}} = .577D \qquad \text{Equation 17}$$

Hulteen *et al.* investigated the effects of the nanosphere diameter and the mass thickness on the size of the nanoparticles [17]. Silver was deposited over a glass substrate. Seven different sizes of nanospheres were used to observe the effect of the nanosphere's size on the periodic particle array. They also compared the structural parameters found from the simple geometric model of the mask against those measured from AFM. The nanoparticle structural parameters measured by the AFM were in good agreement with the geometric predictions [17]. Their study showed that the periodic particle structures with certain shapes and sizes can be fabricated by selecting proper size and mass thickness of nanospheres using the NSL technique. The results of their study are listed in Table 1.

Table 1. Structural Parameters for Ag Nanoparticles Formed from Single Layer Mask [17].

D(nm)	d(nm)	Predicted		Experimental	
		d_{ip}	a(nm)	d_{ip}	a(nm)
542 ± 7	18	312 ± 7	126 ± 7	309 ± 9	153 ± 6
401 ± 7	18	231 ± 7	93 ± 7	229 ± 10	121 ± 6
264 ± 8	40	152 ± 8	62 ± 8	152 ± 5	95 ± 4
264 ± 8	22	152 ± 8	62 ± 8	152 ± 5	80 ± 3
264 ± 8	13	152 ± 8	62 ± 8	152 ± 5	68 ± 4
165 ± 3	18	95 ± 3	38 ± 3	95 ± 2	49 ± 2

3.1.3 Optical Properties of Nanoparticles

Since the optical properties of nanoparticles are important for SERS, much attention has been given for their study. If light with a certain frequency is incident on the surfaces of nanoparticles, it excites the conduction electrons of the particles generating a plasma [18]. This optical property is called Localized Surface Plasmon Resonance (LSPR). This property is specifically evident for the noble metal nanoparticles. At the wavelength of the extinction maximum, all the conduction electrons start to oscillate collectively. If the extinction maximum wavelength is resonant with the frequency of the incident light, the intensity will be greatly increased [18]. Localized Surface Plasmon Resonance (LSPR) of noble metal nanoparticles depends on the size, shape, and external dielectric properties of the nanoparticles [19].

Jensen *et al.* investigated the factors affecting the LSPR of Ag nanoparticles [20]. UV-vis spectroscopy was used to view the LSPR of nanoparticles. Their examination showed that the LSPR of Ag particles can be manipulated over the visible range from 400 to 800 nm of the electromagnetic spectrum as shown in Figure 14 [20]. In Figure 14, plots marked as F, G, and H were generated when the in-plane width of the nanoparticles were varied keeping the shapes and out-of-plane height of Ag particles constant. It can be seen that with the increase of the in-plane width value, the extinction maximum shifts to longer wavelengths. In Figure 14 for D, E, H, and the out-of plane height of the Ag particles were changed keeping the in-plane diameter and shape constant. With the increase of the out-of plane height, the extinction maximum wavelength decreases. C

and F are SERS spectrum taken before and after annealing of the nanoparticle array structure respectively. The LSPR peak maximum underwent a 223 nm blue shift upon annealing [20]. Due to annealing, nanoparticles dewet the substrate.

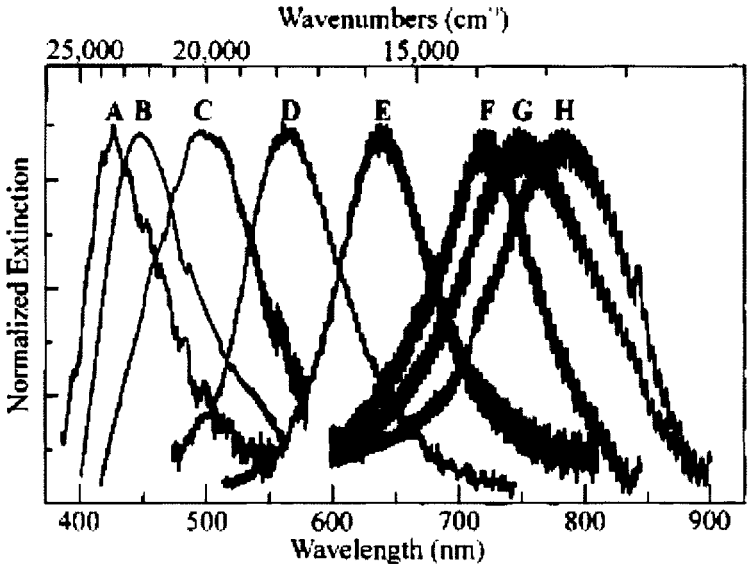

Figure 14. UV-vis extinction spectra of Ag nanoparticles arrays on mica substrate [20].

The results of their study are summarized in Table 2, where elliptical sized particles are represented by E and the triangular by T. The sharpness of their observed LSPR spectra of Ag nanoparticles are reflected by the quality factor Q. The quality factor is determined by the Equation 18, where Γ is the LSPR bandwidth.

$$Q = \frac{\lambda_{max}}{\Gamma} \qquad \text{Equation 18}$$

It is observed that the estimated value of Q is within the range from 5.11 to 7.61.

Table 2. Properties of Ag Nanoparticle from the UV-vis Extinction Measurement [20].

	A	B	C	D	E	F	G	H
In-plane shape	E	E	E	T	T	T	T	T
Extinction maximum λ_{max} (nm)	426	446	497	565	638	720	747	782
Quality Factor Q	6.78	5.77	5.11	6.37	7.19	7.61	5.39	6.20

Jensen *et al.* also studied the LSPR's of Ag particles on two different substrates, silicon and germanium [20]. It was found that for the silicon substrate and the germanium substrate the LSPR were 4739 nm and 6042 nm respectively [20]. Germanium has a higher dielectric constant than that of the silicon, which contributes to the shifting of the LSPR of Ag particles to longer wavelength in the electromagnetic spectrum. This indicates the contribution of the external dielectric environment of the nanoparticles on their optical properties.

In a separate study, Jensen *et al.* investigated the effects of dielectric overlayers on the LSPR of Ag particles. Ag particles were encapsulated with SiO_x overlayers. It is revealed from their study that the LSPR peak shift increases with the increase of the thickness of SiO_x overlayer which is shown in Figure 15 [20].

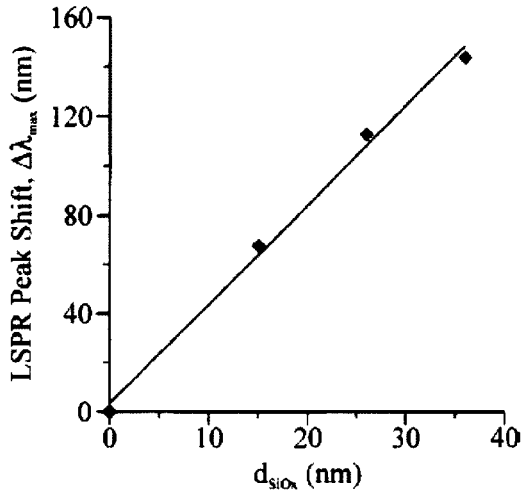

Figure 15. Plot of LSPR peak shift vs. thickness of SiO_x overlayer [20].

3.1.4 Metal Nanoshell

Metal nanoshells are made of a dielectric core (40~250 nm radius) covered by a thin metallic shell (10~30 nm). Generally silica is used for the core dielectric. The plasmon resonance frequency typically shifts to longer wavelength than that for the individual nanosphere [21]. J. B. Jackson *et al.* investigated the effects of the

morphology of the shell surface on optical properties [22]. They explored three different methods to produce the outer silver shell. Depending upon the methods the morphology varies from smooth and uniform to rough to extremely sharp needlelike protrusions. They made a comparison of the optical properties of these nanoshells with various surface roughness with the Mie scattering theory.

In one method, they added varying amounts of gold decorated silica into solution of 1.2 ml Acacia (500 mg/L) with a 0.2 ml buffer solution (1.5 M citric acid, 0.5 M sodium citrate, p^H=3.5) and 0.3 ml of silver lactate. 0.3 ml of Hydroquinone was added as a reducing agent for the silver ions. Citrate solution and Acacia stabilize the silver ions. As a result, the kinetics of the silver reduction becomes slow and the silver shell becomes very rough with needlelike silver spikes [22]. Figure 16 (a) shows the TEM image of the very rough nanoshell. The UV/vis spectra is shown in Figure 16 (b) where curves 1-4 represent spectra for increasing silver thickness. Broad and featureless spectra were found without any distinct maxima. The spectra shows some plasmon like feature which shifts to shorter wavelength when the thickness is increased.

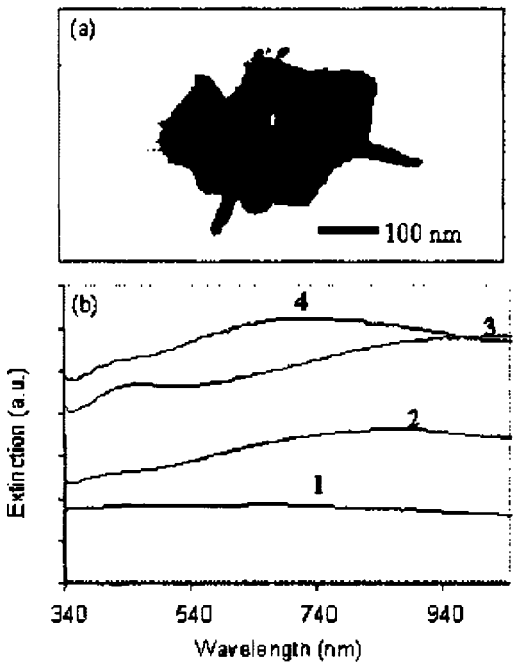

Figure 16. (a) TEM image of the silica particle, (b) UV/vis spectra of increasing silver deposition [22].

In the second method, they mixed gold-decorated silica with a 0.17 mM silver nitrate. Then they added n-propyl gallate (NPG) solution and 4.7 mM NH_4OH. They used the NPG solution as a reducing agent. The amount of silver nitrate which led to different optical extinction spectra are shown in Figure 17 (a). There was a competing reaction which forms silver colloid and hinders the silver deposition. TEM (Transmission Electron Spectroscopy) image is shown in Figure 17 (b). The surface of the shell looks bumpy. With the increase of metal deposition, the magnitude of the extinction spectra increases and surface plasmon begins to shift to longer wavelength.

In the third method, they mixed the gold-decorated silica particles with 0.15 mM solution of silver nitrate. A small amount of formaldehyde was added to begin the reduction of silver ions onto the gold particles on the surface of silica particles. NH_4OH causes rapid p^H change of solution and ensures the reduction of silver ions and their deposition onto the nanoparticle surface. Nucleation of additional silver colloid was hindered. This method produces smooth complete silver nanoshell. The UV/ vis spectra is shown in Figure 17 (a). TEM images before and after the p^H change is shown in Figure 17 (b). Their examination revealed that the plasmon resonance can be tunable through the visible and near infrared wavelengths [22].

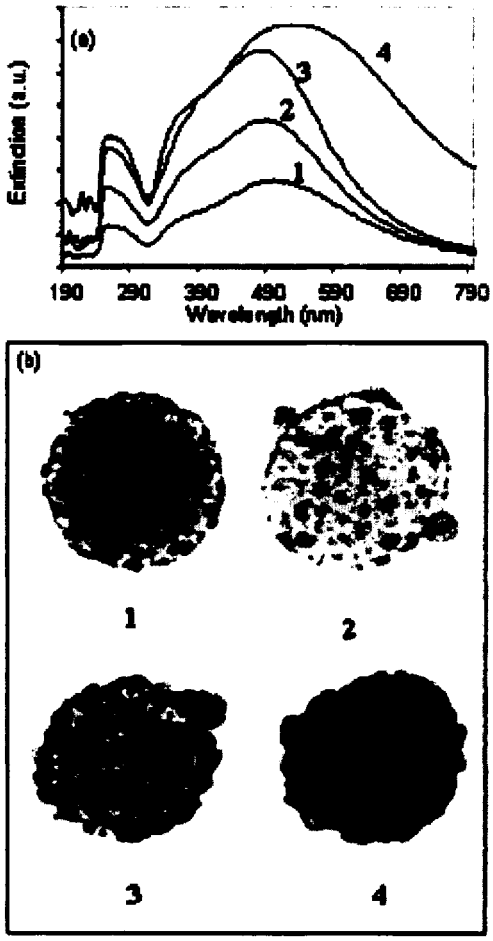

Figure 17. (a) UV/vis spectra of silica particles produced by method 2 and (b) TEM image of the silica particles [22].

3.2 Self-Assembled Material as a Template

3.2.1 DNA as a Template

Gang Wei *et al.* reported a one step synthesis method of silver nanoparticles using DNA network as a template [6]. Rhodamine 6G solution was used to determine the

effectiveness as a SERS substrate. λ DNA solution was dropped onto the APTES (3-Amino Propyl tri Ethoxy Silane) treated mica substrate. The DNA self-assembles into a porous network. Silver ions were impregnated into the DNA network by immersing the substrate into silver nitrate solution. Then the adsorbed silver ions were reduced in sodium borohydride solution. They also investigated the effects of reducing time on the nanoparticle morphology as well as Raman intensity. 1 min, 5 min, and 10 min reducing times were studied. The effects of the diameter size on reducing time are shown in Figure 18.

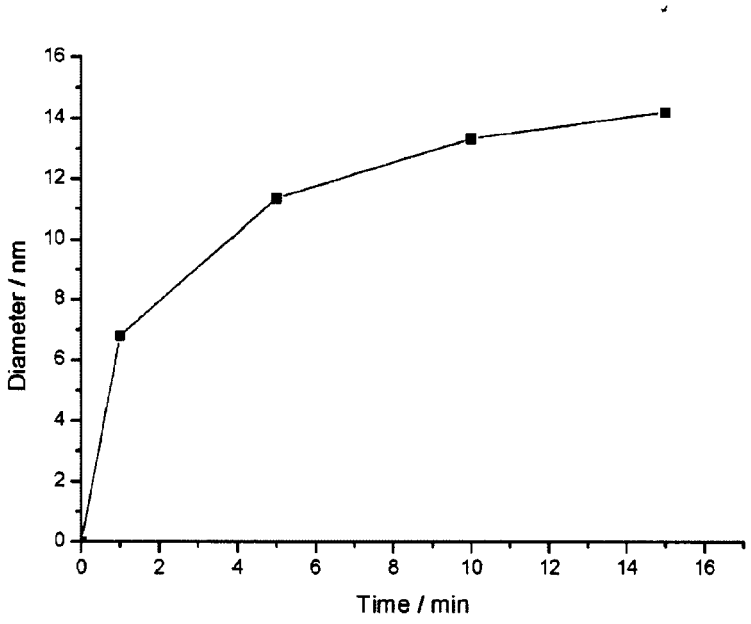

Figure 18. The effects of the diameter size on reducing time [6].

The statistical analysis of the silver particle diameter is shown in Table 3.

Table 3. Statistical Analysis of the Diameter of the Nanoparticles and DNA Network [6].

	Diameter (nm)	Standard Deviation
DNA network	39.49	10.29
Nanoparticles (1 min)	6.79	0.61
Nanoparticles (5 min)	11.35	1.40
Nanoparticles (10 min)	13.54	1.74

Their study revealed that the metal nanoparticles grew on the strands of the DNA network. This is because the electrostatic interaction between the negatively charged backbone of the DNA and the positive charge of the silver hinders the mobility of the DNA strands. For a 1 minute reducing time, silver particles grew uniformly. With an increase of time, silver particles can move along the DNA strands and aggregate. SERS spectra of $1x10^{-8}$ M Rodhamine 6G on the samples are shown in Figure 19.

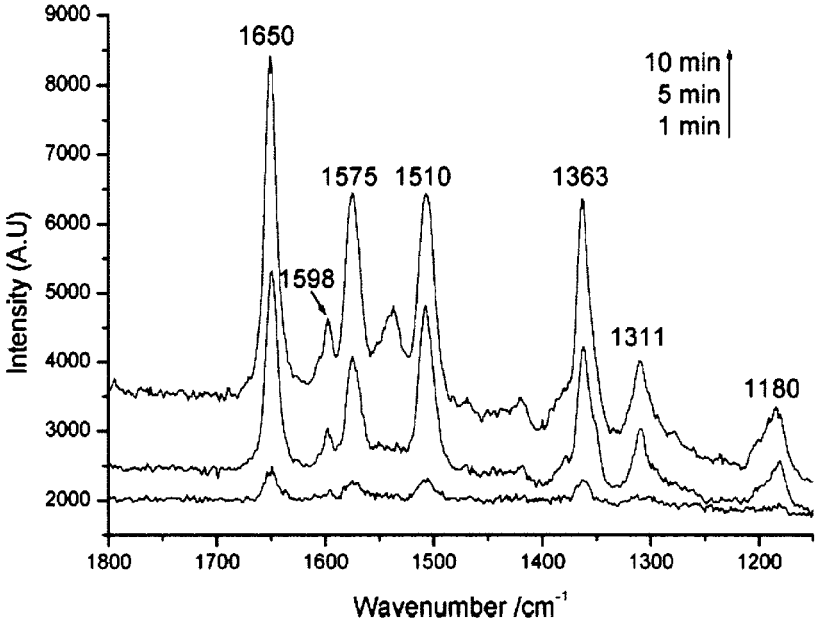

Figure 19. SERS spectra recorded for the samples treated with different reducing time [6]

It shows the enhancement increases with the reducing time. SERS intensity increases with the increase of the mean diameter of nanoparticles. Samples treated with 5 minutes and 10 minutes reducing times have 10 fold and 6 fold Raman enhancement relative to that with of 1 minute.

3.2.2 Diblock Copolymer as a Template

Diblock copolymers are promising for being used as a template due to their nature of self-assembly and ease of processing [23]. Obtaining a good quality film in short time is a prime objective of template processing. Kathryn W. Guarini *et al.* investigated the effects of the different processing parameters such as anneal time, temperature and the film thickness on the self-assembly process. They measured pore size, shape, and

separation to characterize the process. They used Polystyrene-Poly Methyl Meth Acrylate (PS-PMMA) diblock copolymer film on silicon. Sample preparation involves three steps. First the substrate surface was pretreated with random copolymer to make the surface neutral to the two polymer blocks. Then the thin film was spin-coated on the substrate from dilute solution of PS-PMMA in toluene. Film was annealed to promote the self-assembly into a hexagonal array of PMMA cylinders in PS matrix [23].

Anneal temperature can control the speed of self assembly of diblock copolymer. Diblock anneal temperature was varied between 140^0C and 200^0C while maintaining a fixed anneal time to observe its effect on self-assembly process. For 180^0C and one hour anneal time it was observed that the film quality is superior to those achieved at 165^0C after 24 hour annealing [23].

Figure 20a, 20b, and 20c show the self-assembled film quality on anneal temperatures which are 140^0C, 165 ^{0}C, and 180^0C respectively. Anneal time was one hour. Figure 20d shows the variation of pore diameter and center to center spacing as a function of anneal temperature. The variation of both qualities of the film significantly drops at higher anneal temperature.

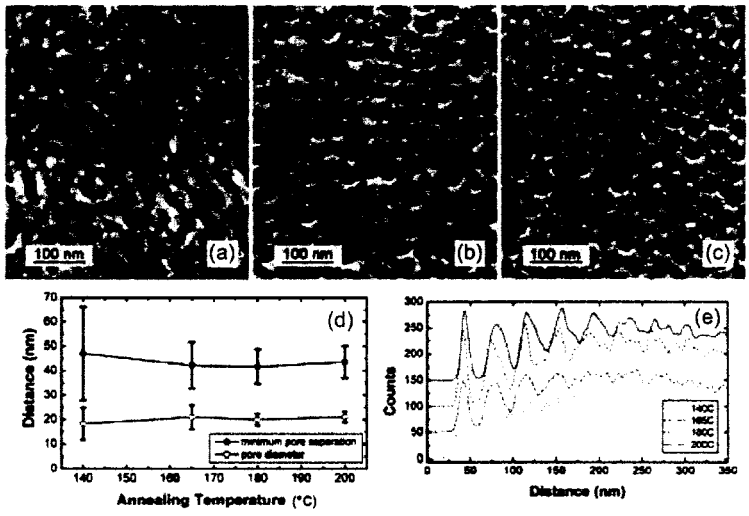

Figure 20. SEM images of the self-assembled film for three annealing temperature (a) 140^0C, (b) 165^0C, (c) 180^0C, (d) Pore diameter and center-to-center spacing as a function of anneal temperature, and (e) Spectra of interpore spacings [23].

The diblock copolymer film should have a very uniform nanometer scale domains so that it can be used as a template for nanostructure fabrication. The film thickness has an optimum value for which such uniformity can be achieved. The film thickness depends on spin speed and molecular weight. Figure 21a, 21b, and 21c show the films of 31 nm, 42 nm, and 51 nm thickness respectively. As seen from the SEM images, too thin film (31nm) and too thick (51 nm) film have no regular domain shape as well as uniformity. Figure 21d shows the Gaussian distribution of pore diameters. Thus it can be concluded that there is an optimum range of film thickness for which maximum uniformity can be achieved [23]. Too thick and too thin films have a wide range of distribution in pore diameter. 42 nm thick film shows maximum uniformity.

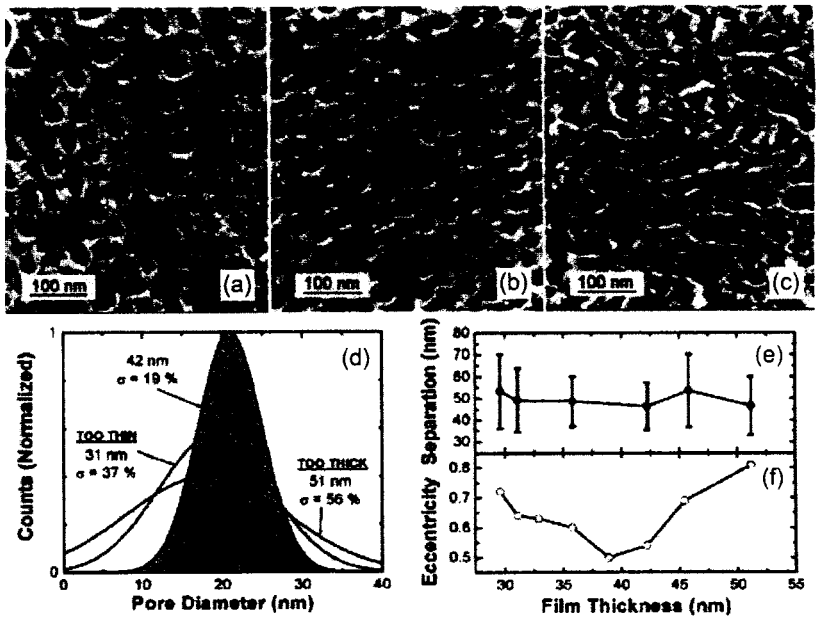

Figure 21. SEM images for three different film thicknesses: (a) 31 nm, (b) 42 nm, (c) 51 nm, (d) Gaussian fits of pore diameter distribution for the three film thicknesses, (e) Nearest neighbor spacing, and (f) pore eccentricity versus film thickness [23].

Pore diameter and separation distance are determined by fundamental properties of the polymer. These two basic template dimensions are determined by total copolymer molecular weight keeping the molecular weight ratio constant. Limin Cao *et al.* in their experiment formed PS-PMMA diblock copolymer with two different molecular weights: 67000 g/mol and 132000 g/mol. The molecular weight ratio was 70:30 PS/PMMA. Figure 22a and 22b show the 67 kg/mol and 132 kg/mol polymer film consists of smaller pores (mean diameter 20 nm) than the 132 k polymer (mean diameter 30 nm). The thickness of the film also depends on molecular weight. It was reported that the 67

kg/mol film was 56 nm thick. The mean center to center spacing are 42 nm and 62 nm for 67 kg/mol and 132 kg/mol films respectively.

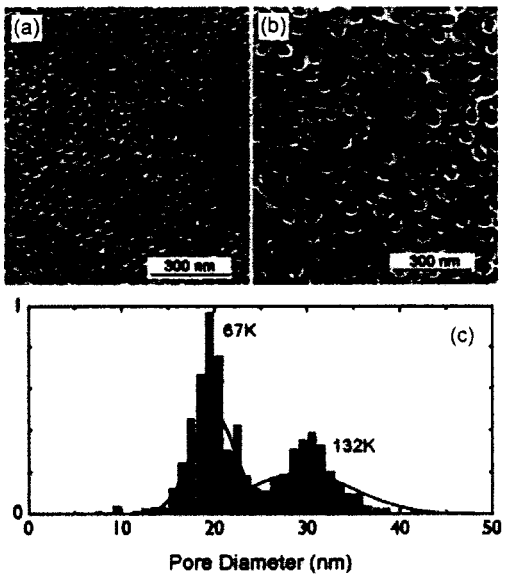

Figure 22. SEM images for the effects of molecular weight in template dimension (a) 67k g/mol (b)132 k g/mol, and (c) Histograms of the pore diameter distribution with Gaussian fits for the two molecular weights [23].

3.3 Summary

For metal coated nanosphere substrates, maximization of the SERS intensity depends on the optimization of the processing parameters such as silver film thickness, nanosphere diameter, and excitation wavelength. The optical properties of the nanoparticles depend on the nanoparticle size, shape, and dielectric properties of the surrounding media. For DNA templated silver periodic particle array substrates, the SERS intensity depends on the diameter of the metal nanoparticles.

CHAPTER 4

EXPERIMENTAL PROCEDURE

4.1 Overview of Experiments

Surface-enhanced Raman Spectroscopy (SERS) with extremely high sensitivity can be used to detect a fingerprint of any organic molecule [1]. Surface-enhanced Raman signals of a target analyte can be obtained when the analyte is placed on the surface of a substrate with noble metal nanoparticles or rough noble metal surface. The large electric fields created at the surface of the noble metal under laser illumination enhance the Raman signals of the analyte. The objective of this research was to develop a process to prepare a substrate with nanoparticle arrays that can be used for SERS. The work was divided into two basic parts: (i) preparing the silver nanoparticle arrays on a known substrate using nanoporous material as a template, and (ii) using SERS as a diagnostic tool with Ag nanoparticle arrays. This proved their applicability for SERS.

For part (i) of the experiment, two different approaches were taken to prepare substrates using self-assembled nanoporous polymer material. PS-PFEMS (Poly Styrene-Poly Ferrocenyl Ethyl Methyl Silane), a diblock coploymer, was used as a template to prepare silver nanoparticle arrays on silicon covered with thermal oxide substrates. Experiments were also conducted to create silver nanoparticle arrays on APTES (3-Amino Propyl Tri Ethoxy Silane) treated mica substrates using λ-DNA as a template.

For part (ii) of the experiment, silver coated silica nanosphere substrates were prepared to observe SERS signal for different types of analytes. The goal of studying these samples was to determine the proper protocol for achieving valid SERS spectra from Ag arrays. This protocol was used to validate the effectiveness of Ag arrays generated in part (i) of the experiment.

4.2 Fabrication of Silver Nanoparticle Array Using PS-PFEMS Diblock Copolymer

4.2.1 Silicon Substrate Preparation

Three inch diameter, (111) silicon wafers were cleaned according to the standard wet chemical procedure to remove any organic and metallic impurities. A sequence of three chemical baths were used to clean the six wafers which are as follows: (i) Piranha solution (2:1 96% sulfuric acid: 30% Hydrogen peroxide) (ii) RCAI solution (1:1:5 NH_4OH: H_2O_2:H_2O) (iii) RCA II solution (1:1:5 HCl :H_2O_2 :H_2O). Each of the chemical baths was followed by a 1 minute dip in 5% HF solution and a rinsing step in deionized water. The sulfuric acid solution removes organic contaminants and oxidizes the surface. The HF dip removes the surface silicon dioxide and sets impurities free. RCAI step removes the organic films and metal particles like Au/, Ag/, Cu/, Ni/, Cd/, Zn, Cr, and Co. RCAII removes alkaline ions like K, Na, and other metals such as Al, Fe, and Mg removed by etching. A thick thermal oxide layer was grown on all six of the cleaned wafers using Calogic Systems LPCVD (Low Presssure Chemical Vapor Deposition chamber) configuration. Oxide growth was done in a wet oxygen environment. During

the run hydrogen and oxygen rate were 7.5 slm and 4.0 slm respectively. A 160 nm thick thermal oxide layer was grown at 1000^0C for 27 minutes.

4.2.2 Polymer Deposition

Four substrates were cleaned with Piranha solution just prior to the polymer deposition to remove the organics. Then they were soaked in Venyl Methyl Silane (VMS) solution for 4 minutes. The solution was prepared by pouring six drops of VMS uniformly into a solution of 570 ml IPA and 30 ml deionized water. VMS acts as an adhesion promoter for the subsequent polymer deposition. VMS replaces the OH^- group of the thermal oxide substrate surface by a methyl group and transforms the surface from hydrophilic to hydrophobic. The effectiveness of the VMS as an adhesion promoter was determined by measuring the contact angle before and after the treatment. An FTA (Model 100 Series/VESA) contact angle tool was used for the measurement. Surface energy was determined by applying the Owens Wendt model using the measured contact angle. The details of the Owens Wendt model will be discussed in Chapter 5 when the results are presented. Adhesion between the polymer film and the substrate is critical. Otherwise dewetting will occur [6].

A solution of PS-PFEMS which was synthesized via sequential living anionic polymerization in toluene was deposited on four silicon substrates using a spin coater. The morphology of the polymer film on the substrate depends on the film thickness and the volume of the PS-PFEMS in the solution. The film thickness was controlled by the spinning speed. The film thickness is inversely proportional to the spin speed. The

volume fraction of PS- PFEMS in solution was 26 vol%. Four different spin speeds of 1000 rpm, 2000 rpm, 3000 rpm, and 4000 rpm were used for polymer deposition. One sample per spin speed was used. Bulk morphological studies on the material confirmed the speed which is required to form PFEMS cylindrical microdomains on the PS matrix. AFM was used to characterize the morphology of the samples. The speed that produces the cylindrical domains of PFEMS in PS matrix was chosen to prepare thin film of polymer on the remaining two silicon substrates. This resulted in 3 wafers with the cylindrical domains which were cut into seven pieces, creating 21 samples.

After spin coating, the samples were solvent annealed for two days. All the samples were kept under a glass covered environment where twenty vials of toluene solution were kept open. The vials were kept open so that the vapor of toluene can reach the surface of the sample and help to rearrange the morphology.

4.2.3 Etching of PFEMS

The deposited PFEMS cylindrical domains were etched out from the PS matrix to create a nanohole array. PFEMS etching was done by breaking the Si-C bond bridging between the PS and the PFEMS. Three different types of wet etching were tried. In one chemistry, iodine in methanol solutions of different concentrations were used. Etching time was varied. The etching time and conditions are summarized in Table 1. Iodine oxidizes the Fe in PFEMS. Then I_3^- ions are formed. There is a polarity difference between C and Si present in the PFEMS. I_3^- ions are attracted to the positive polarity in C and break the bond between C and Si. Soaking in solution followed by degassing in

vacuum was done to help the PFEMS part of the matrix to come out. Because of the capillary effect the PFEMS may trap inside the PS matrix. The degassing treatment was performed to overcome that effect.

A second chemistry of hydrogen peroxide with ascorbic acid was also used as wet etchant, Table 4. In this solution, high energetic OH radicals formed in the solution will eventually attack the Fe in PFEMS [24]. A third chemistry involved exposing the film to UV light (375 nm wavelength) for ten minutes and then soaking them in NaOH/MeOH based iodine solution, Table 4.

Table 4. Summary of the Etching Experiments.

Sample	Etchants	Etching time	Concentration
Sample_1	I_2 in MeOH	1 hr	0.05M
Sample_2	I_2 in MeOH	2 hr	0.05M
Sample_3	I_2 in MeOH	8 hr	0.05M
Sample_4	I_2 in MeOH	overnight	0.05M
Sample_5	I_2 in MeOH	1 hr	0.89M
Sample_6	I_2 in MeOH	2 hr	0.89M

Sample	Etchants	Etching time	Concentration
Sample_7	I_2 in MeOH	8 hr	0.89M
Sample_8	I_2 in MeOH	overnight	0.89M
Sample_9	I_2 in MeOH (degas and vacuum effect)	2 hr	0.89M
Sample_10	I_2 in MeOH (degas/vacuum effect)	overnight	0.89M
Sample_11	H_20_2 with Ascorbic Acid	10 min	20mM
Sample_12	H_20_2 with Ascorbic Acid	2 hr	20mM
Sample_13	I_2 in MeOH:NaOH solution	2 hr	0.5gm (1:10 ml NaOH:MeOH)
Sample_14	I_2 in MeOH:NaOH solution	overnight	0.5gm (1:10 ml NaOH:MeOH)
Sample_15	I_2 in MeOH:NaOH solution	2hr	0.5gm (2:10 ml NaOH:MeOH)
Sample_16	I_2 in MeOH:NaOH solution	overnight	0.5gm (2:10 ml NaOH:MeOH

Sample	Etchants	Etching time	Concentration
Sample_17	UV, I_2 in MeOH:NaOH solution	24 hr	0.5gm (2:10 ml NaOH:MeOH
Sample_18	UV, I_2 in MeOH:NaOH solution	42 hr	0.5gm (2:10 ml NaOH:MeOH)

Following the etch, the films were analyzed to determine if the etch was successful. The PS part of the diblock copolymer is UV-ozone active and the PFEMS part is inactive due to the presence of the inorganic iron [25]. UV-ozone was used to volatilize the organics and produce the oxide of inorganics. If there was PFEMS left after the etch, the UV-ozone would convert the PFEMS to iron oxide particles. AFM images were taken after the UV-ozone procedure to determine the presence of iron oxide nanoparticles. One sample was kept as a control for the AFM. That sample was untreated with the etchants and used for comparing the treated sample roughness data. This assumes that the surface roughness detected by the AFM would be due to the presence of metal oxides left on the sample. If there are iron oxides present, they would have the same pattern as the diblock copolymer they came from. This destructive measurement provided the information about whether the etching successfully removed the PFEMS or not. After etching each sample was cut into four pieces. One piece of

each sample was used for destructive analysis. Two AFM images were taken per each sample at two scan sizes 1 μm x 1 μm and 10 μm x 10 μm.

4.2.4 Silver deposition

After getting the nanoporous polymer film, silver was deposited on the three pieces of the successfully etched silicon sample using an E-beam evaporator (CHA Vacuum Evaporator, Model SEC-1000-RAP). 5 nm silver was deposited on two samples at $7.4x10^{-7}$ torr pressure at 3 Å/sec deposition rate. 10 nm silver was deposited on one sample. For control samples, 5 nm and 10 nm silver were deposited on two pieces of bare silicon covered with a 160 nm thermal oxide. The use of the E-beam evaporator ensures the uniform deposition of silver.

4.2.5 Lift-off

The PS part of the silver film with 5 nm deposited silver samples were soaked in a toluene solution. Soaking in 12 hours and 24 hours were tried for lift-off. The samples were ultrasonicated in toluene solution for 10 minutes prior to the soaking in toluene. Toluene was chosen because both of the polymeric blocks of the PS-PFEMS diblock copolymer are soluble in toluene. It created silver nanoislands on the silicon substrate. SEM was used for the morphological analysis of the sample.

4.3 Synthesis of Silver nanoparticles using λ - DNA

Six freshly cleaved mica substrates were treated with APTES (3-aminopropyl-triethoxy silane). APTES functionalizes the mica substrate by immobilizing the DNA strands. Moreover, it makes the substrate positively charged [6]. As a result, the silver ions being adsorbed by the subsequent steps will be electrostaticaly repelled by the APTES which is positively charged and attracted to the negatively charged λ-DNA network. To create a uniform λ DNA network on APTES treated mica, λ DNA solution in pure water was pippetted out on the samples and then dried naturally in air. Different DNA strands self-assembled to form uniform reticulated structures.

In order to study the effects of the reducing time on the particle size, two samples were prepared using 20 ng/µl DNA solution. 20 µl of DNA solution were pippetted out in each of the samples and then dried in air. Then they were soaked with a 10 mM $AgNO_3$ solution for 30 minutes. Silver ions were adsorbed on the nanoporous DNA network due to the electrostatic interaction between the silver ions and phosphate backbone of DNA strands. Then the samples were subsequently reduced in a $NaBH_4$ solution. The reducing times are 5 min and 10 min for the samples named dna_1 and dna_2 respectively.

Another sample was prepared using 50 ng/µl DNA solution. In this case a 20 µl DNA solution was applied and dried on mica twice to create the DNA network with higher concentration of DNA strands. A total of 40 µl DNA solution was used on a mica substrate to study the effect of concentration of DNA on particle size. This sample is

named dna_3. The reducing agent's concentration and time were .01 wt% and 10 minutes respectively.

To investigate the effects of the concentration of the DNA solution on the particle size, two samples were prepared using 50 ng/μl and 148 ng/μl DNA in water solution. Other processing conditions such as concentration of $NaBH_4$ (0.005 wt%) and reducing time (20 min) were kept the same. These samples are named dna_4 and dna_5.

At the end of each step, the substrates were rinsed with 50% ethanol-water solution. Table 5 summarizes all the processing parameters used to prepare five samples. Morphological analysis was done using AFM. Raman measurements were done using 1 ppt nicotine solution.

A sixth sample was prepared by following the parameters of that sample which showed the maximum Raman enhancement signal. The sixth sample was cut into two pieces for experiments to remove the DNA network. One piece was treated in eight hours UV-ozone and the other one for one hour oxygen plasma followed by reducing in sodium borohydride solution (.005 wt%, 10 min) to remove the DNA.

Table 5. Summary of Processing Parameters.

Sample	λ-DNA concentration (ng/μl)	Volume of λ-DNA solution (μl)	Concentration of $NaBH_4$ (wt%)	Reducing time (min)
dna_1	20	20	0.01	5
dna_2	20	20	0.01	10
dna_3	50	2x20	0.01	10
dna_4	50	2x20	0.005	20
dna_5	148	2x20	0.005	20

4.4 SERS experiments

Silver coated silica nanosphere samples on glass slides were prepared to observe the surface enhanced Raman signals for different analyte solutions. Glass substrates were cleaned according to the published literature procedure described by Van-Duyne [18]. A solution of sulfuric acid and chromerge (1:1 volume ratio) was prepared. Then the glass

slides were dipped into the solution for 5 minutes and rinsed with deionized water. After cleaning they were stored in deionized water. Sample preparation involved two steps. First, 300 nm silica nanospheres were deposited on the glass slide using a spin coater. Five different speeds of 500, 2000, 3000, 3500, and 4000 rpm were used. One sample per each speed was prepared. 10 μl deionized water was used for dilution while spinning the solution of silica beads on the glass slide. Second, silver was deposited using an E-Beam evaporator. 75 nm silver was deposited on each sample at 3Å/sec deposition rate.

Raman measurements were done on each of the samples. Deionized water, 1 ppt nicotine solution, and 1-octadecanethiol were used as analytes. Two spots of each sample were used for analysis. Raman spectra were analyzed in order to get a valid peak for the analyte molecules. SEM was used for morphological analysis.

4.5 Instruments

Tapping mode atomic force microscopy (AFM) imaging was performed on a Digital Instruments dimension 5000 AFM (DI, Santa Barbara, CA) equipped with an E-scanner. Scanning Electron Micrographs were taken from JEOL 6400F SEM. Raman spectra were collected with a Renishaw InVia Raman microscope (Renishaw Ltd., Gloucestershire, United Kingdom). The Raman signals were collected with conventional 90^0 geometry. A thermoelectrically-cooled CCD was used for detection. Radiation of 514.5 nm and 488 nm from a water cooled argon ion laser were used for the SERS excitation.

CHAPTER 5

RESULTS

Silver nanoislands were prepared on silicon covered with 160 nm thermal oxide using PS-PFEMS diblock copolymer template. Silver nanoparticles were also synthesized on mica substrate using λ-DNA as a template. Later the DNA template was removed. Morphology of silver nanoparticle arrays were analyzed using standard microscopy techniques: SEM and AFM. Raman spectroscopy was then done to determine the effectiveness of these silver nanoparticle arrays as SERS substrates.

5.1 Analysis of Silver Nanoparticle Array using PS-PFEMS Template

5.1.1 Effectiveness of VMS as an Adhesion Promoter

The silicon substrates covered with 160 nm thermal oxide were treated with VMS (Venyl Methyl Silane) prior to the polymer deposition. VMS was used as an adhesion promoter. Adhesion between the polymer film and the substrate is critical. Otherwise delamination will occur. The contact angle between the silicon substrate and test liquid was measured before and after the VMS treatment to determine the effects of VMS on the substrate. An FTA (model 100 Series/VESA) contact angle tool was used for the measurement. Surface energy was determined by applying Owens/Wendt model using the measured contact angles [26].

According to Owens and Wendt model surface energy of a solid has two components. One of them is dispersive component which is basically a non-site specific

interaction between the solid and the applied liquid. The second component is polar component which accounts for the variation in site specific interaction. Similarly, Owens Wendt is also a two-component model for liquid surface energy. Figure 23 is the graphical representation of the Owens and Wendt model.

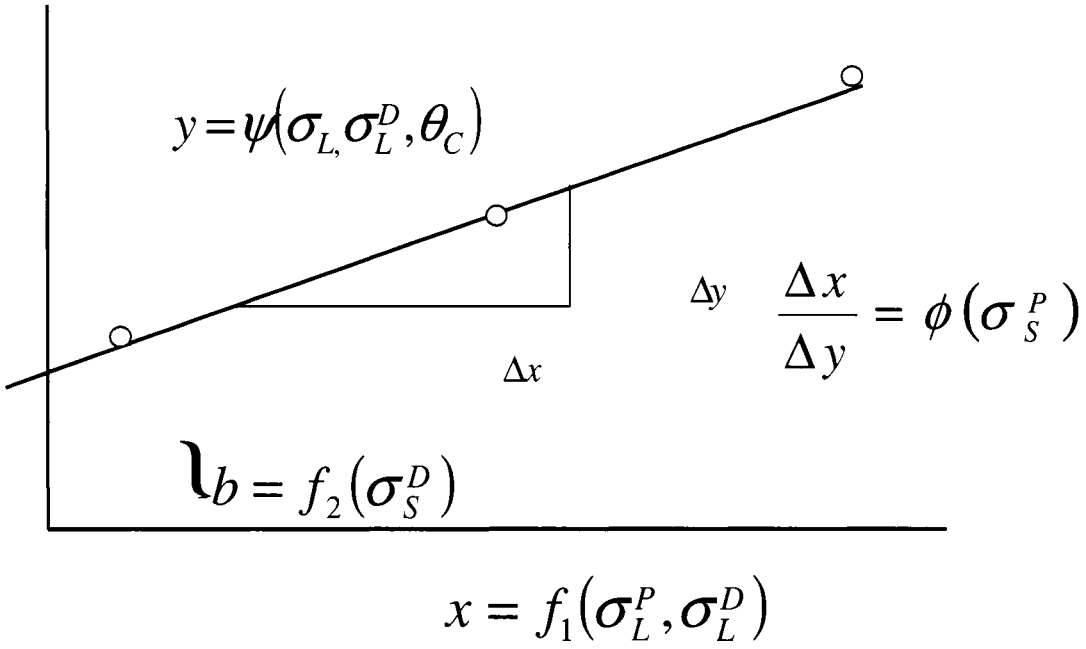

Figure 23. Graphical representation of Owens and Wendt model.

Wherein:

θ_C = Contact angle between probe liquid and solid

σ_S^D = Dispersive component of the surface energy of the solid

σ_S^P = Polar component of the surface energy of the solid

σ_L^P = Polar component of the surface tension of probe liquid

σ_L^D = Dispersive component of the surface tension of probe liquid

σ_L = Overall surface tension of probe liquid.

Equation 19 to 22 are used to calculate surface energy of solid from contact angle measurements using probe liquid.

$$y = \frac{\sigma_L(\cos\theta + 1)}{2\sqrt{\sigma_L^D}} \qquad \text{Equation 19}$$

$$\text{slope, } m = \sqrt{\sigma_S^P} \qquad \text{Equation 20}$$

$$x = \frac{\sqrt{\sigma_L^P}}{\sqrt{\sigma_L^D}} \qquad \text{Equation 21}$$

$$\text{intercept, } b = \sqrt{\sigma_S^D} \qquad \text{Equation 22}$$

Overall surface tension, the dispersive, and the polar component of surface tension of some liquids are determined experimentally. These liquids are called probe liquids. In this experiment, three different probe liquids water, cyclohexane, and toluene were used. In this experiment contact angle between the probe liquid and the silicon substrate (before and after VMS treatment) were measured. Table 6 shows the standard data used for the probe liquids. Table 7 shows the measured contact angles between the probe liquid and the substrate (before and after the VMS treatment).

Table 6. Used Data for the Probe Liquids.

Probe Liquid	Surface Tension σ_L (mN/m)	Polar Component σ_L^P (mN/m)	Dispersive Component σ_L^D (mN/m)
Water	72.8	26.4	46.4
Cyclohexane	25.5	25.5	0
Toluene	28.4	26.1	2.3

Table 7. Measured Contact Angle Data.

Probe liquid	Contact Angle (degree) (Before VMS)	Contact Angle (degree) (After VMS)
Water	0	59.71
Cyclohexane	26.01	19.3
Toluene	14.28	3.25

Using data from Table 6 and Table 7, the Owens and Wendt model was applied to obtain the plot of Figure 24, where x and y coordinates are determined using Equation 3 and Equation 1 respectively.

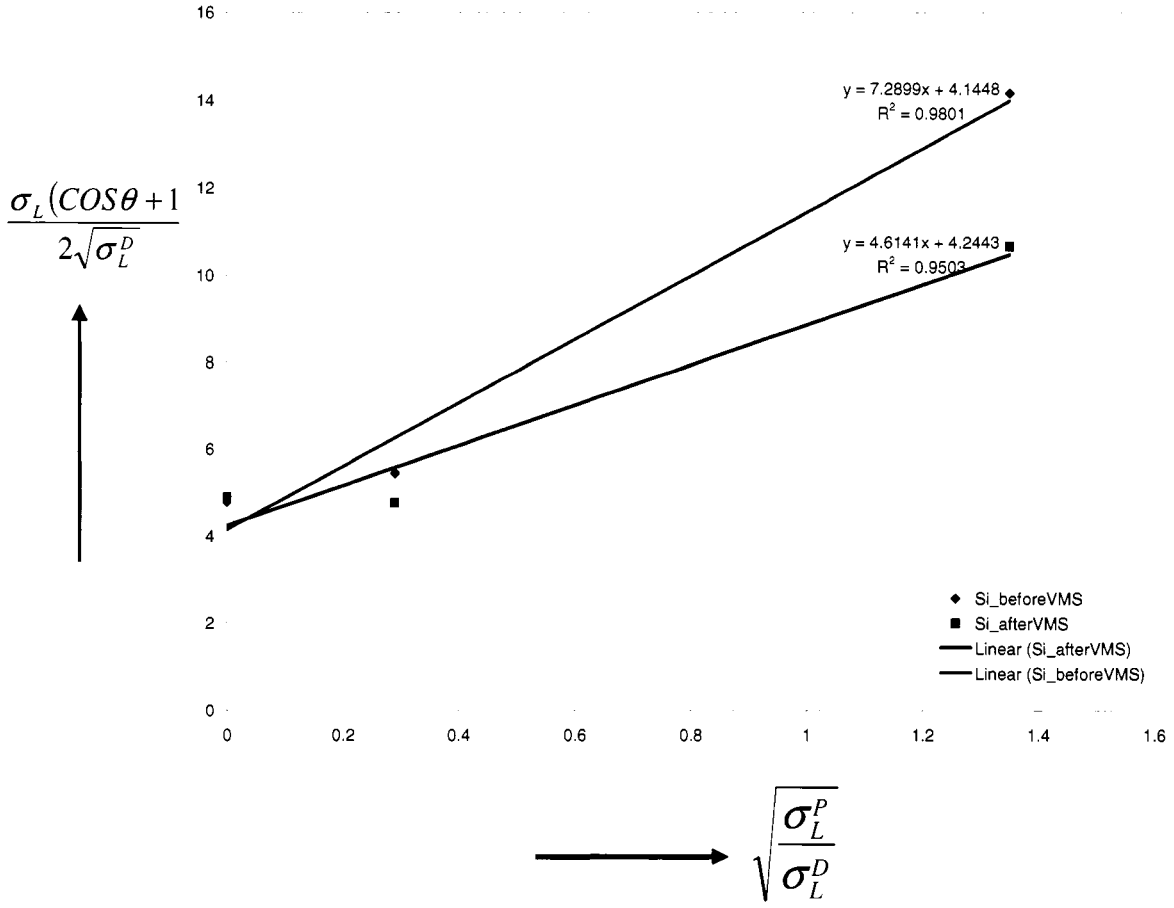

Figure 24. Owens/Wendt plot of silicon substrate.

Slope (m) and intercept (b) were obtained by using standard linear curvefit technique from the data points. Using these data in Equation 3 and Equation 4, polar and dispersive components of surface energy of silicon were obtained. Table 8 shows the obtained data of surface energy of silicon before and after VMS treatment.

Table 8. Summary of Obtained Surface Energy Data of Silicon.

Condition	Slope	Intercept	Polar component σ_S^P (mJ/m^2)	Dispersive component σ_S^D (mJ/m^2)	Surface Energy σ_S ($\sigma_S^P + \sigma_S^D$) (mJ/m^2)
Untreated with VMS	7.28	4.14	52.99	17.13	70.12
Treated with VMS	4.61	4.24	21.25	17.97	39.22

The overall surface energy of Si before and after the VMS treatment are 70.12 mJ/m^2 and 39.22 mJ/m^2 respectively. After VMS treatment surface energy of the silicon is reduced by 44%. Reduction in surface energy ensures good adhesion between the polymer film and the substrate.

5.1.2 Analysis of Polymer Film on Silicon Substrate

In this experiment, PS-PFEMS (Polystyrene-Poly Ferrocenyl Ethyl Methyl Silane) diblock copolymer was used as a template to control the size of the nanoparticles. The cylindrical domains of PFEMS in PS matrix serve that purpose. The PFEMS domains in the PS matrix can be perpendicular or parallel to the surface depending on the film thickness and the volume fraction of PS-PFEMS in the solution. Polymer deposition was done by using four different spin speeds 1000, 2000, 3000, and 4000 rpm on silicon

covered with a 160 nm thermal oxide. After polymer deposition, surface morphology of these samples were characterized using an AFM. Whether the PFEMS domains are perpendicular or parallel to the substrate are clearly discernable in the AFM phase image. Figures 25 and 26 show the AFM phase images of the diblock copolymer film prepared at the 1000 and 2000 rpm spin speed

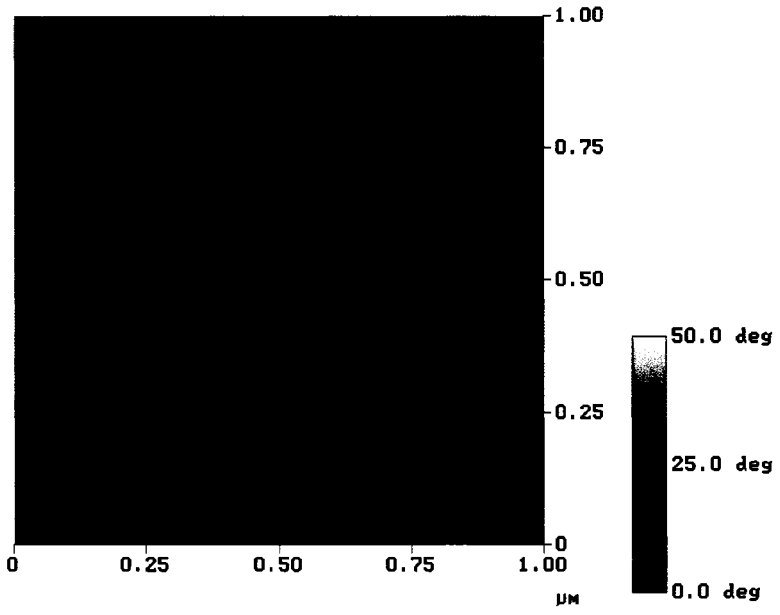

Figure 25. AFM phase image of the PS-PFEMS film on silicon prepared at 1000 rpm spin speed.

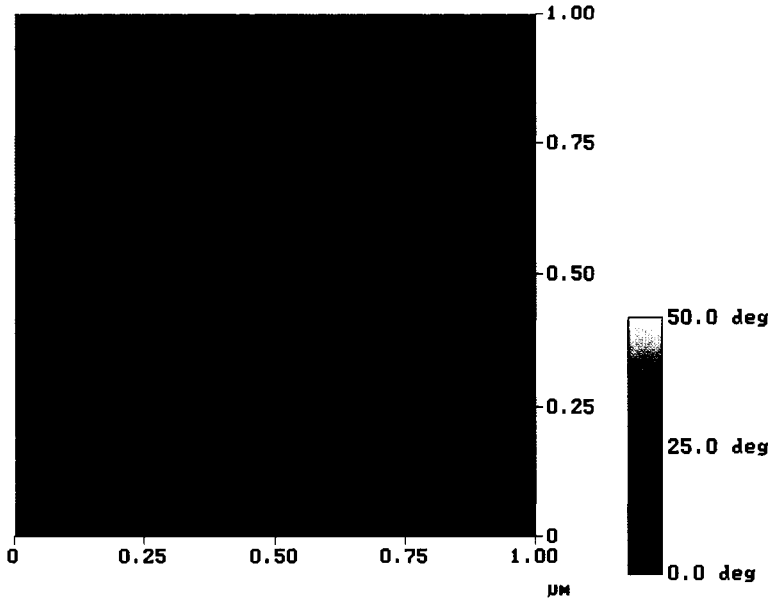

Figure 26. AFM phase image of the PS-PFEMS film on silicon prepared at 2000 rpm spin speed.

Figure 25 shows the phase image of polymer film where PFEMS domains are parallel to the substrate which was obtained at 1000 rpm spin speed. Figure 26 shows the combination of perpendicular and parallel domains of PFEMS in the PS matrix which was obtained at 2000 rpm spin speed. The dark part and the light part in each AFM (tapping mode) image represents PFEMS and PS respectively. The phase image of the polymer film prepared at 3000 and 4000 rpm spin speed are shown in Figures 27 and 28 respectively. Figure 28 shows the cylindrical PFEMS domains lying perpendicular to the silicon substrate.

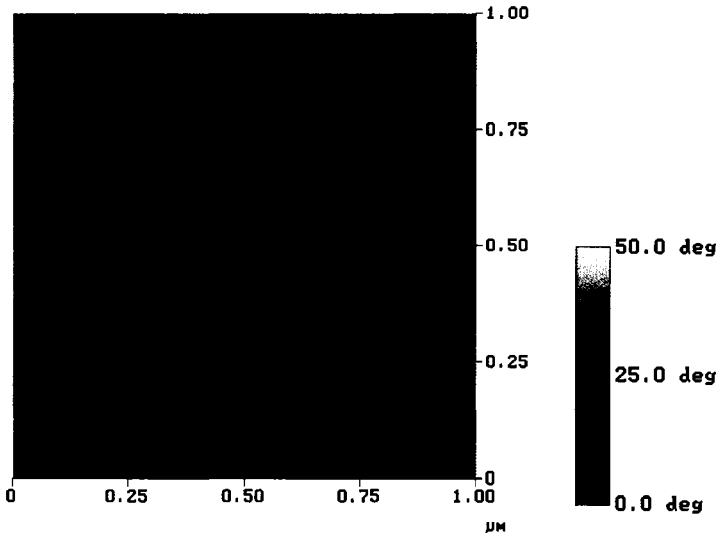

Figure 27. AFM phase image of the PS-PFEMS film on silicon prepared at 3000 rpm spin speed.

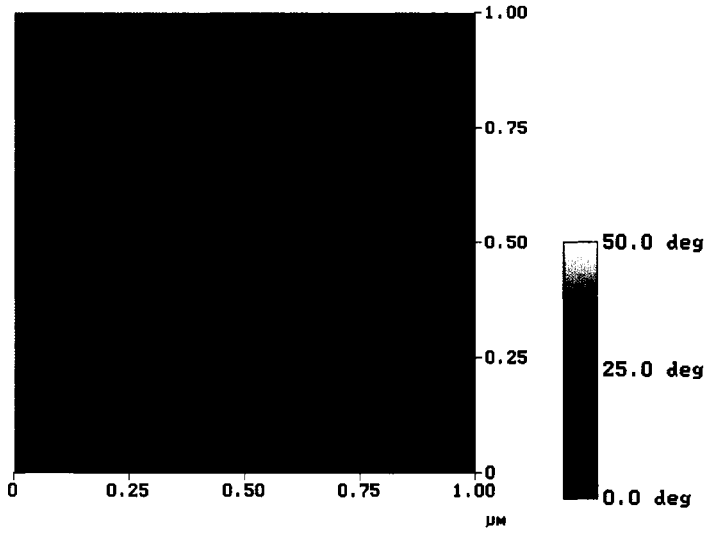

Figure 28. AFM phase image of the PS-PFEMS film on silicon prepared at 4000 rpm spin speed.

Figure 28 shows the zoomed in images of a small area on samples prepared at different spin speeds. This zoomed in images help to study the morphology of the grown polymer film at different spin speeds qualitatively. In Figure 29, the dark (black) arrow marked regions indicate the PFEMS domains that are lamaeller (parallel to the substrate) and the bright (white) arrow marked regions indicate the cylindrical (perpendicular to the substrate) domains of PFEMS. At 1000 rpm spin speed, the PFEMS domains are only lamaeller. As the spin speed is increased to 2000 rpm and 3000 rpm, some of the PFEMS domains become cylindrical, resulting in a mixture of parallel and perpendicular domains. At 4000 rpm, all of the PFEMS domains are cylindrical.

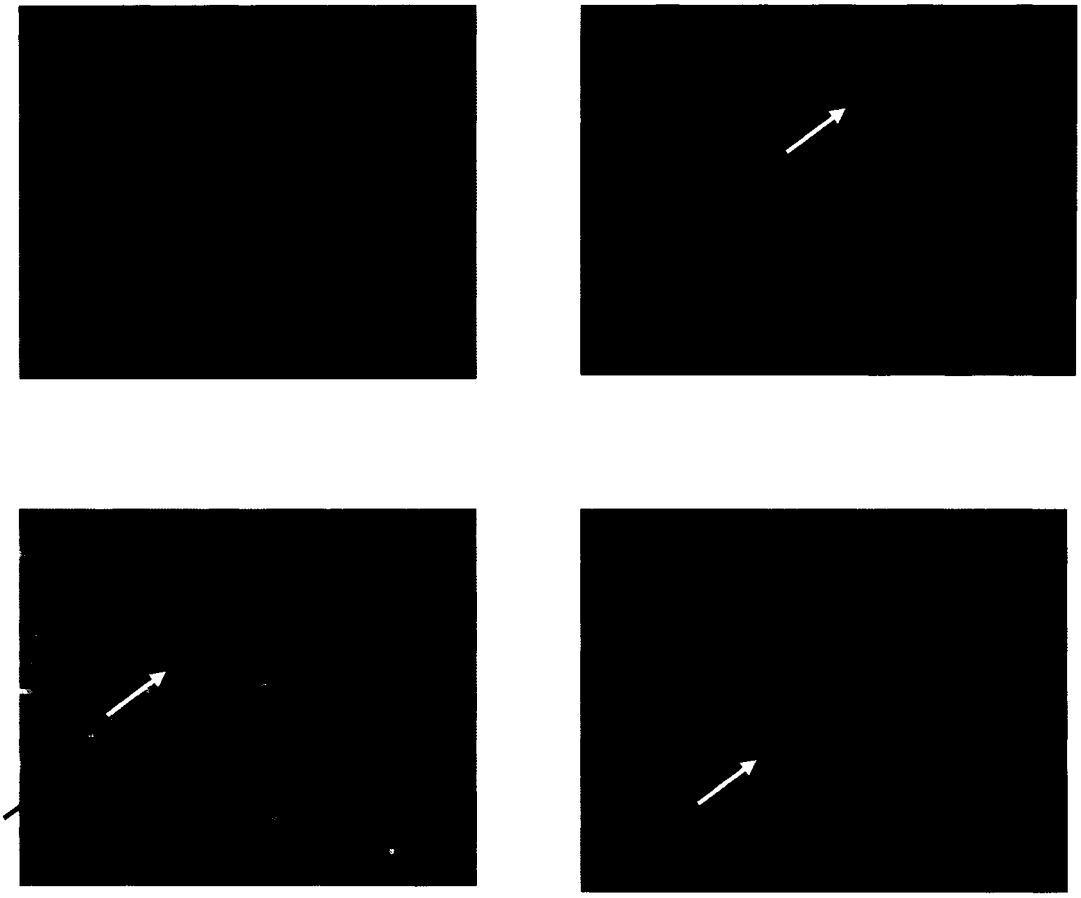

Figure 29. Zoomed in images of a section of samples prepared at different rpm.

5.1.3 Etching of PFEMS

Etching of PFEMS in films such as shown in Figure 28 creates a nanohole array in the PS matrix. Three different types of wet etching were tried to determine the etching process which completely removes the PFEMS. (i) Iodine in methanol solutions of different concentrations were used. (ii) Hydrogen peroxide with ascorbic acid was used as wet etchant of PFEMS. (iii) Ten minutes UV exposure (375 nm wavelength) followed by Iodine in methanol/sodium hydroxide based solution was used. After etching, each

sample was treated with UV-ozone. Ozone volatilizes all the organics leaving the oxide particles of inorganics. After UV-ozone, AFM image was used to characterize the surface morphology of the sample. Cross-sectioning of AFM image using software of the tool provides the roughness data. Comparison between the roughness data of the etched sample with the controlled one tells about the extent of the completeness of etching. This destructive way was used to evaluate the completeness of etching of PFEMS.

One sample was kept as a control. No etching was done on that sample. The average roughness of the control sample is 5.747 nm. AFM images were taken at three different spots of each sample. The mean roughness at 95% confidence level and the relative standard deviation of the samples prepared are shown in Table 9.

Table 9. Summary of the Etching Experiments.

Sample	Etchants	Etching time	Concentration	Mean roughness (nm)	Rel.St. Dev. (%)
Sample_1	I_2 in MeOH	1 hr	0.05M	5.727	19.69
Sample_2	I_2 in MeOH	2 hr	0.05M	5.67	20.05
Sample_3	I_2 in MeOH	8 hr	0.05M	4.95	18.07
Sample_4	I_2 in MeOH	overnight	0.05M	4.386	17.35
Sample_5	I_2 in MeOH	1 hr	0.89M	5.02	16.89
Sample_6	I_2 in MeOH	2 hr	0.89M	5.01	27.89
Sample_7	I_2 in MeOH	8 hr	0.89M	4.30	30.56
Sample_8	I_2 in MeOH	overnight	0.89M	4.26	35.69
Sample_9	I_2 in MeOH (degas and vacuum effect)	2 hr	0.89M	5.02	18.98
Sample_10	I_2 in MeOH (degas/vacuum effect)	overnight	0.89M	4.20	24.60
Sample_11	H_20_2 with Ascorbic Acid	10 min		inconclusive	
Sample_12	H_20_2 with Ascorbic Acid	2 hr		inconclusive	
Sample_13	I_2 in MeOH:NaOH solution	2 hr	0.5gm (1:10 ml NaOH:MeOH)	4.89	17.32
Sample_14	I_2 in MeOH:NaOH solution	overnight	0.5gm (1:10 ml NaOH:MeOH)	3.05	18.89
Sample_15	I_2 in MeOH:NaOH solution	2hr	0.5gm (2:10 ml NaOH:MeOH)	4.56	14.23
Sample_16	I_2 in MeOH:NaOH solution	overnight	0.5gm (2:10 ml NaOH:MeOH)	2.84	10.84
Sample_17	UV, I_2 in MeOH:NaOH solution	24 hr	0.5gm (2:10 ml NaOH:MeOH)	2.42	16.12
Sample_18	UV, I_2 in MeOH:NaOH solution	42 hr	0.5gm (2:10 ml NaOH:MeOH)	0.233	40.32

Comparing with the roughness data of the control sample, it is seen from Table 4 that roughness did not decrease for most of the samples except sample_16. For sample_17 treated with iodine solution shows the 53% decrease of roughness which means the absence of iron oxide particles as well as PFEMS. That means the etchant (0.5 gm iodone in 2:10 NaOH: MeOH) worked better than the rest of the others to remove PFEMS. The sample treated 42 hr (sample_18) shows 95.94% reduction in roughness compared to the control sample. The relative standard deviation observed 40.32%. It indicates the completeness of etching for 42 hr.

Two more samples were treated with that etchant. The AFM height image of the control sample is shown in Figure 30. The AFM height images of the sample_17 and sample_18 are shown in Figure 31 and 32 respectively.

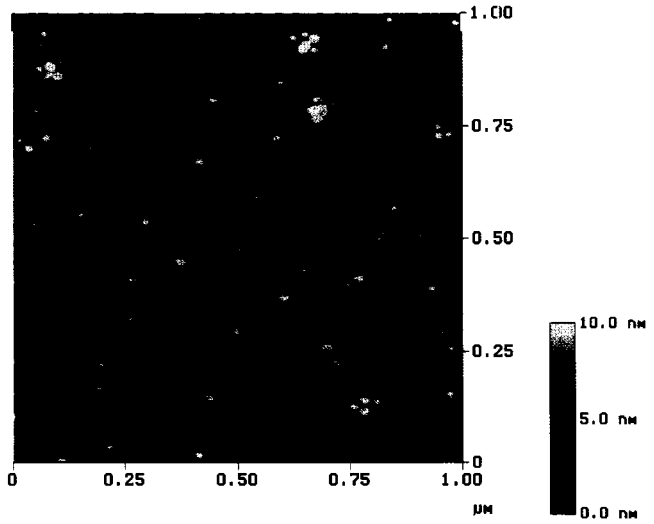

Figure 30. AFM height image of control sample.

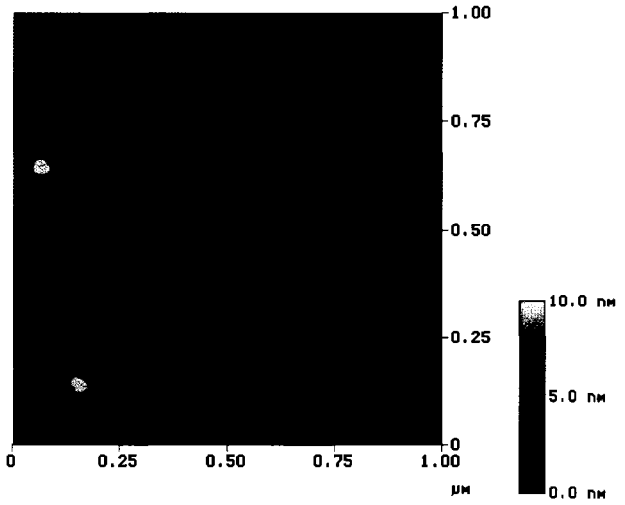

Figure 31. AFM height image of the sample_18 which is etched by soaking 24 hr.

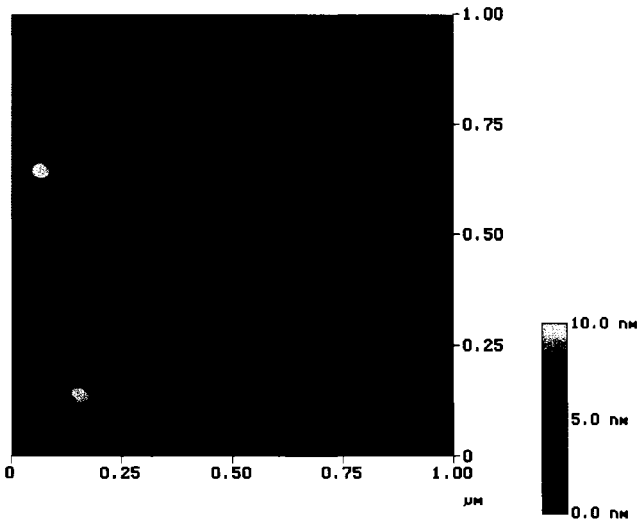

Figure 32. AFM height image of the sample_18 soaked in 42 hr.

For further confirmation, AES (Auger Electron Spectroscopy) analysis was done on the samples. The atomic concentration of the elements that are present in the samples found from AES are documented in Table 10. Absence of Fe in the sample_18 confirms that the PFEMS part in PS matrix was completely etched out.

Table 10. Summary of Auger Electron Analysis Data.

Component	Sample_17 (at %)	Sample_18 (at %)
C	6.08	5.32
O	43.86	44.46
Si	49.62	50.22
Fe	0.44	< 0.01

5.1.4 Analysis on Metal Deposition and Lift-off

5 nm silver was deposited on the etched sample (sample_18). Silver particles will be deposited in the etched PFEMS pores. The remaining PS part of the polymer template will also be covered by thin silver film deposited on it. Lift-off of this PS part of the polymer will remove everything leaving silver particles on the substrate.

Toluene was used for lift-off because the block copolymer components are soluble in toluene. After lift-off the sample was characterized with SEM. Figure 33 shows the scanning electron micrograph of sample_18 after lift-off.

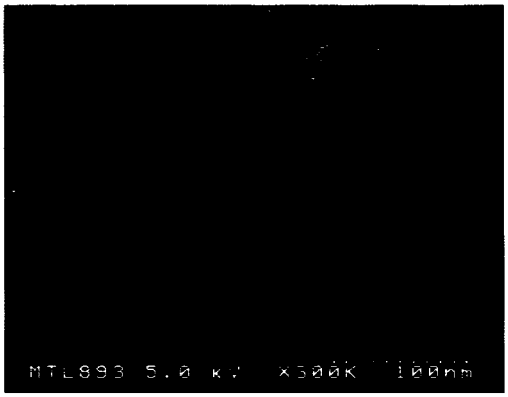

Figure 33. Scanning Electron Micrograph showing the Ag nanoisland on Si.

It is clear from the SEM image that the size of the nanoislands of silver are not uniform. Average size is 27.6 nm with standard deviation 7.23 nm. The sizes were estimated from the SEM image using the image scale. Although the particle shapes are not uniform, they were measured across a horizontal line to provide some basis of comparison.

The size and spacing between the nanoislands depend on the size and periodicity of the PFEMS part of the polymer. In other words, observing the morphology of the polymer film, the arrangements of the array of silver particles can be predicted. Figure 34 is the AFM image of the sample with polymer film before etching. The dark part and the light part represent the PFEMS and PS part respectively.

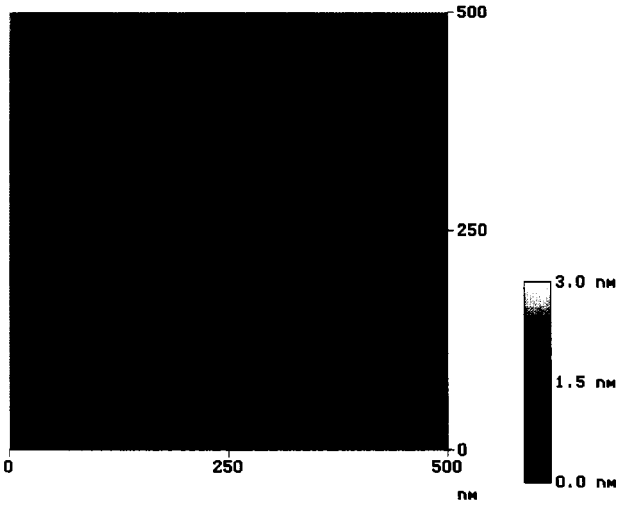

Figure 34. AFM topographical image of polymer film on silicon.

It is obvious from the figure that the periodicity of PFEMS in PS matrix is not uniform. This explains the observed non-uniform spacing between the nanoislands shown in Figure 33.

To confirm whether the nanoislands of silver on silicon are directed by the polymer template or not, two control experiments were done. A 5 nm silver film was deposited on a Si substrate covered with 160 nm thermal oxide. A scanning electron micrograph of the sample is shown in Figure 35. The bright isolated islands in the image are deposited silver on the silicon. Thus 5 nm silver could not be deposited as a conformal film on silicon.

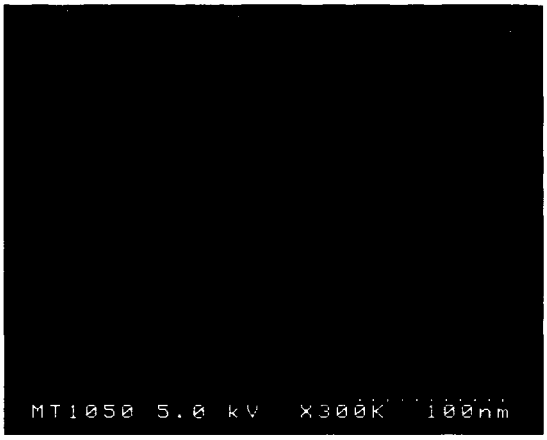

Figure 35. Scanning Electron Micrograph of 5 nm silver on Si covered with 160 nm SiO_2.

10 nm silver was deposited on an already etched sample (sample_18) and then the remaining PS part with silver was lifted-off. A scanning electron micrograph is shown in

Figure 36. The image shows that substrate is covered by a silver film which is the bright part of the image. The isolated dark areas in the image are holes in the silver film exposing the substrate underneath. Since most part of the substrate is covered by the silver film, it shows that the lift-off process was not completed.

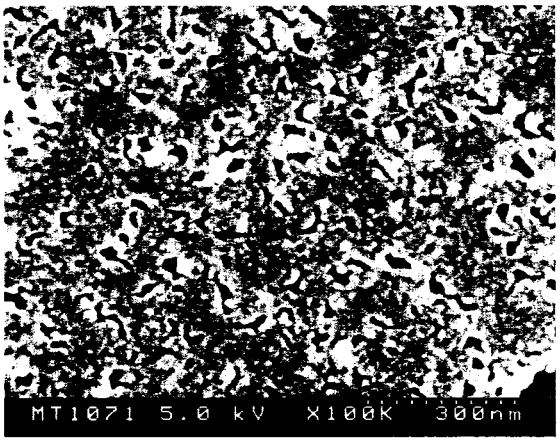

Figure 36. Sample after 10 nm silver deposition and lift-off.

Control on the size of the silver nanoparticles using PS-PFEMS template is limited by the lift-off process. There are some prerequisites for successful lift-off. The deposited silver must be formed as a conformal film and the thickness of the metal film must be approximately one-third of the polymer film thickness [25]. All the samples in this part of the experiment were prepared using 4000 rpm spin speed. The thickness of the PS-PFEMS film deposited on the substrate at that spin speed is approximately 15 nm. 5 nm silver was then deposited. Figure 35 shows that 5 nm of silver is insufficient to

form a conformal film on the sample. On the other hand 10 nm film is too thick to be lifted-off.

The deposited polymer film thickness can not be increased because then it would form parallel PFEMS domains to the substrate instead of cylindrical microdomains. This is a significant processing problem which can not be circumvented.

5.1.5 Results on Raman Measurements

Raman analysis was performed to determine the effectiveness of the sample as a SERS substrate. The laser spot was 1 μm in diameter and excitation source was at a wavelength of 488 nm. Raman spectra were collected on Renishaw Raman microscope (Model InVia) with 5.75 mW laser power and 10 sec exposure time. Raman spectra at dry is used as background. The Raman spectra collected on the sample with 1 ppt nicotine solution are shown in Figure 37 at two different spots. The band around 1030 cm^{-1} represents the nicotine peak. It arises from the breathing mode of nicotine molecule [27]. The peak around 1300 cm^{-1} to 1500 cm^{-1} is due to the presence of an impurity on the sample.

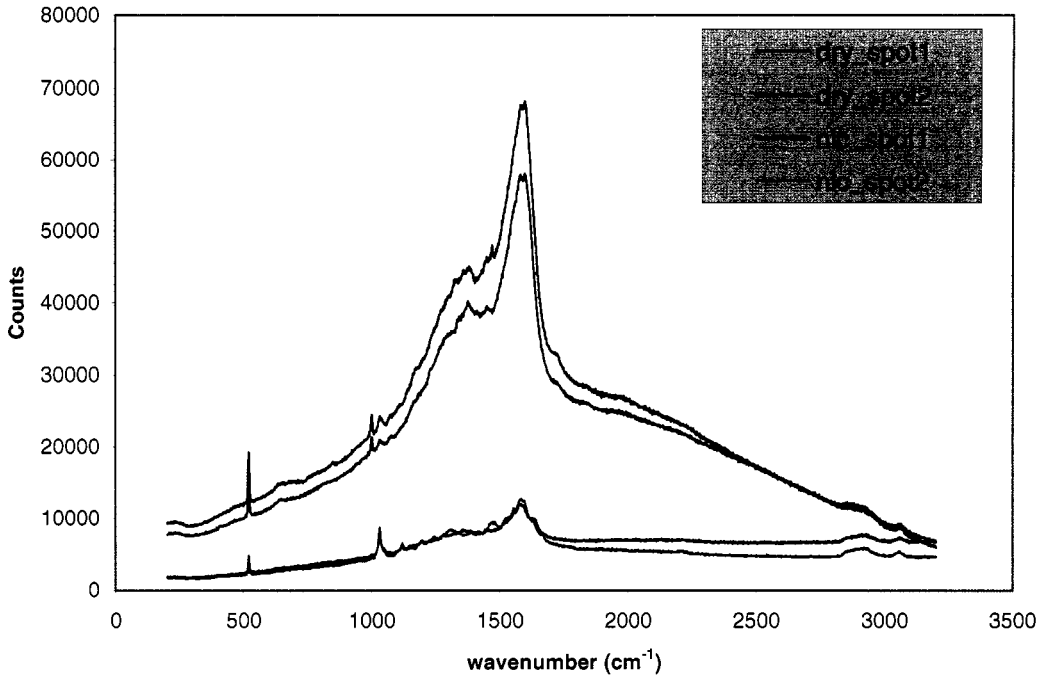

Figure 37. Raman spectra at dry and with 1 ppt nicotine solution of the sample (sample_18).

A 54 μm by 10 μm area was chosen on the sample for mapping. Mapping was done with nicotine solution at 488 nm laser line. Mapping data represents the Raman spectra at the selected area of the sample. Mapping data are shown in Figure 38, where the dark spot represents 7000 counts of nicotine peak and the bright spot represents 8800 counts of nicotine peak.

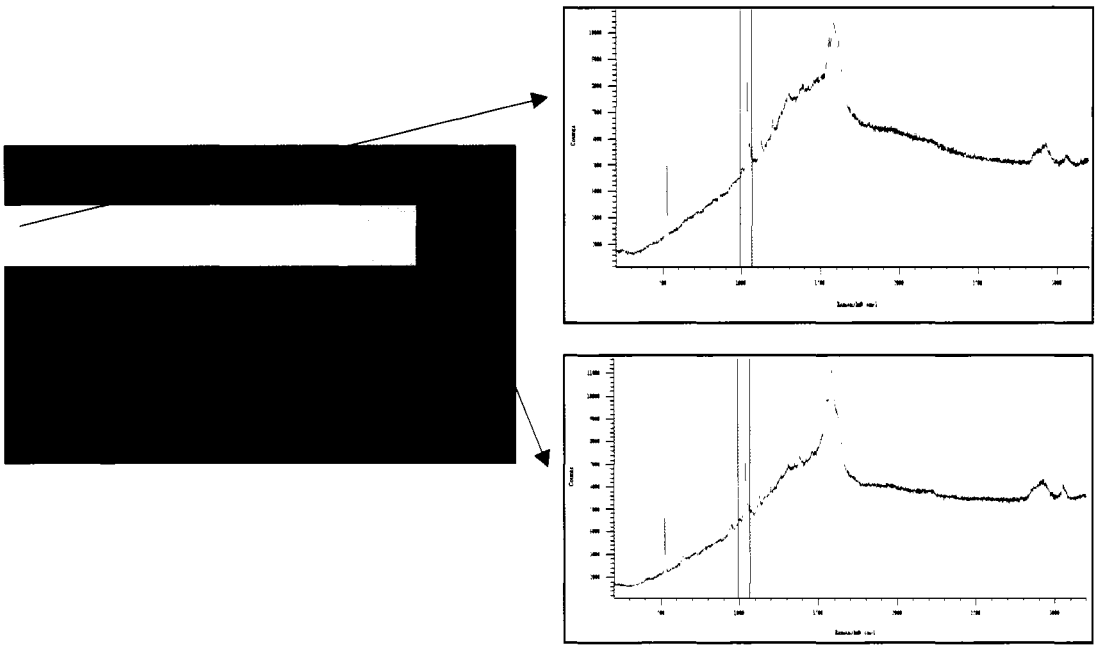

Figure 38. Map of 1030 cm^{-1} nicotine peak on the sample.

SERS spectra were collected of 1 ppt nicotine at 17 different spots on the sample. Mean intensity is 8775 counts with standard deviation 834.66. The high standard deviation value shows the non uniformity of SERS spectra within the sample. The sample is inhomogenious. The particle size and spacing are so random that it can be concluded that the resulting enhancement in Raman signal arise from the silver nanoparticles formed naturally from silver evaporation of thin films, and not from the structure imposed by the block copolymer template.

5.2 Synthesis of Silver Nanoparticles using λ-DNA as a Template

5.2.1 Morphological Analysis

The aspect ratio of a DNA molecule is defined as the ratio of diameter to length. The aspect ratio of a λ-DNA molecule is 16 μm/2 nm. Because of the high aspect ratio, different DNA strands tend to cross-over and form a reticulated structure when they are dried from solution on a substrate [6]. Figure 39 shows the top view of an AFM topographical image of a self-assembled λ-DNA network (10 ng/μl DNA solution) on a mica substrate. In our experiment, the concentration of DNA solution used was 20-148 ng/μl. For these concentrations, the DNA chains and mesh became vague in contrast to that of the mica substrate in AFM image. That is why 10 ng/μl DNA solution was used to take the image of DNA network given in Figure 39.

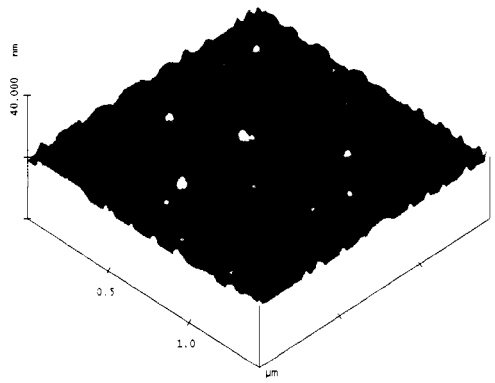

Figure 39. Top view of AFM topographical image of DNA network on mica.

In order to study the effects of reducing time on the particle size, two samples were prepared using 20 ng/μl DNA solution. Then they were soaked with a 10 mM $AgNO_3$ solution for 30 minutes and subsequently reduced in a $NaBH_4$ solution. The reducing time were 5 min and 10 min for the samples named as dna_1 and dna_2 respectively. Three 1μm x 1μm spots were investigated using an AFM. The silver particles were not found at all the spots. AFM analysis was done for one spot per sample where a considerable amount of particles were found. Lateral dimension of the synthesized silver nanoparticles were determined from the section analysis of the AFM topographical images. A statistical analysis of the recorded dimension indicates that the mean particle diameters are 15.90 nm and 70.30 nm for the samples dna_1 and dna_2 respectively. The standard deviation of particle diameters are 4.12 nm and 13.83 nm for the samples dna_1 and dna_2 respectively. As expected, with the increase of reducing time the particle size increases. With the increase of reducing time silver ions will get more time to be move along the DNA strands and become bigger.

To increase the particle density, the volume and concentration of DNA solution were increased. 40 μl DNA solution was used on mica substrate to study the effect of concentration of DNA on particle size. 20 μl DNA solution was applied and dried on mica twice to create the DNA network with higher concentration of DNA strands. The sample dna_3 was prepared using 40 μl of 50 ng/μl DNA solution. The reducing agent's concentration was .01 wt% and time was 10 minutes. Ten different 1 μm x 1 μm spots were investigated using AFM. Estimating the AFM images show that silver particles were formed in all the spots. An example AFM image is shown in Figure 40. All the

spots had similar images. With the increase of the volume of DNA solution used, the particle density increases. This is because with the increase of the volume of DNA solution, more DNA strands could incorporate into the network, so the silver particles got more nucleation sites to be adsorbed. During reduction, they convert to metallic silver nanoparticles. From the section analysis of the AFM topographical images the lateral dimension of the synthesized silver particles was determined. A statistical analysis of the recorded silver nanoparticles indicates that the mean particle diameter is 34 nm. The standard deviation of particle diameter is 9.18 nm.

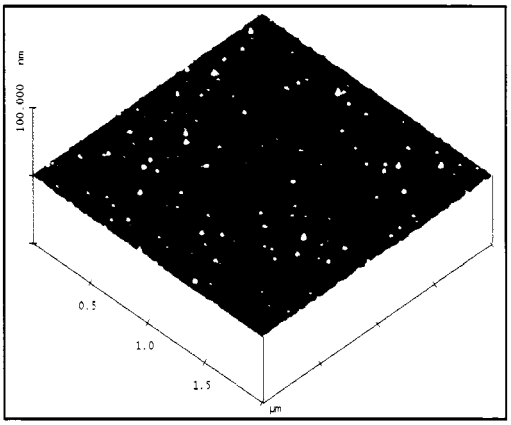

Figure 40. Top view of AFM topographical image of dna_3 sample.

The processing parameters with the obtained particle size are summarized in Table 11. In the samples dna_1 and dna_2, all the parameters were kept constant except the reducing time. It is seen that with the increase of reducing time, the particle size

increases. The formed silver particles are highly dispersed. In comparison between the samples dna_2 and dna_3, it is found that with the increase of the volume and concentration of DNA solution, the particle density increases.

Table 11. Summary of the Processing Parameters of the Samples.

Sample	λ-DNA concentration (ng/μl)	Volume of λ-DNA solution (μl)	Concentration of $NaBH_4$ (wt%)	Reducing time (min)	Particle size (nm)
dna_1	20	20	.01	5	15.90± 4.12
dna_2	20	20	.01	10	70.30± 13.83
dna_3	50	2x20	.01	10	34± 9.18

To investigate the effects of the concentration of the DNA solution on the particle size, two samples were prepared using 50 ng/μl and 148 ng/μl DNA in water solution. Other processing conditions such as concentration of $NaBH_4$ (0.005 wt%) and reducing

time (20 min) were kept the same. The samples are named dna_4 and dna_5. Three different spots per sample were chosen for AFM analysis. The topographical AFM image and section analysis of dna_4 sample are shown in Figure 41 and Figure 42. A statistical analysis indicates that the mean particle size is 590.72 nm. The standard deviation of particle size is 124.49 nm. Some of the particles got aggregated.

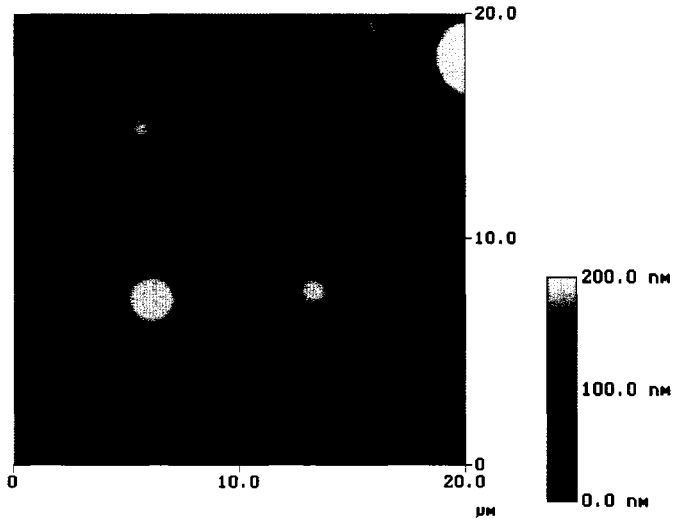

Figure 41. The topographical AFM image of dna_4.

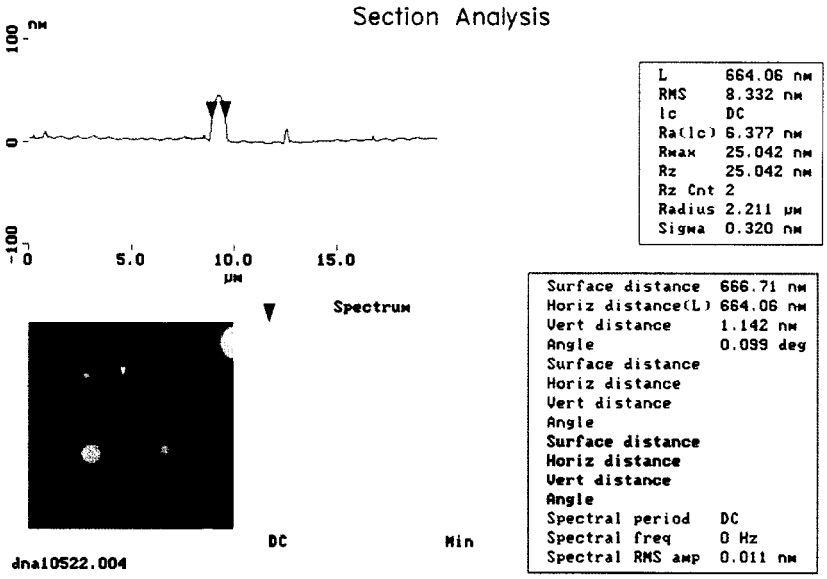

Figure 42. The section analysis of AFM image of the dna_4 sample.

The AFM topographical image and the section analysis of dna_5 sample are shown in Figure 43 and Figure 44 respectively. AFM analysis was done at three different spots of the sample. In dna_5 sample most of the silver nanoparticles were aggregated. From the section analysis the mean lateral dimension of the cluster of nanoparticles is 2.18 µm. The standard deviation is 0.56 µm.

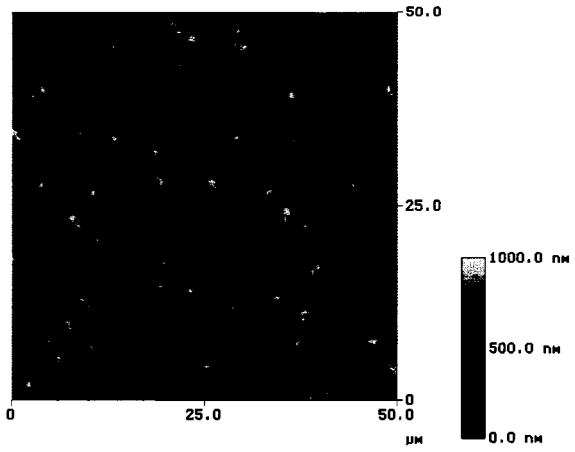

Figure 43. AFM topographical image of dna_5 sample.

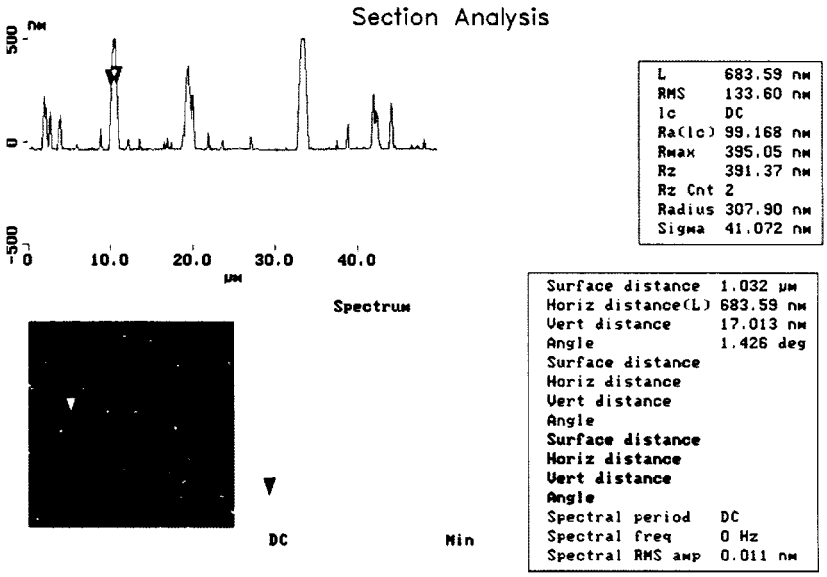

Figure 44. Section analysis of dna_5 sample.

The topographical zoomed AFM image of the dna_5 sample is shown in Figure 45. From the image it is clearly shown that the particles are aggregated. The morophological analysis of dna_4 and dna_5 are summarized in Table 12. Raman measurements were done on all the five samples to find which particle size gives the maximum enhancement.

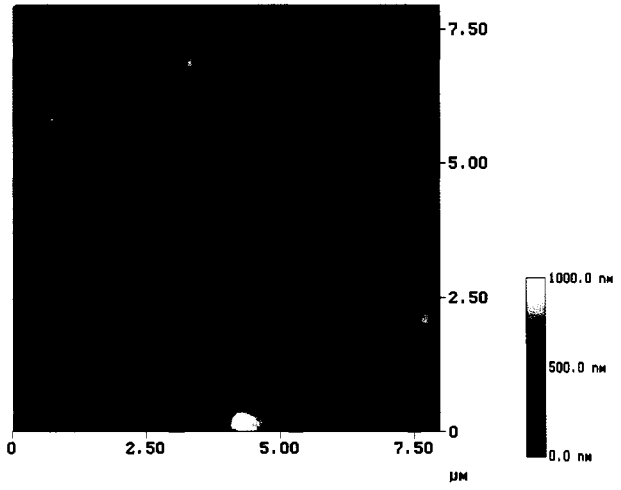

Figure 45. Zoomed topographical AFM image of dna_5 sample.

Table 12. Summary of Morphological Data.

Sample	λ-DNA concentration (ng/μl)	Volume of λ-DNA solution (μl)	Concentration of $NaBH_4$ (wt%)	Reducing time (min)	Particle size (nm)
dna_4	50	2x20	.005	20	590± 124.49
dna_5	148	2x20	.005	20	2000± 560

5.2.2 Characterization for SERS

Raman measurements on dna_1 sample were done at three different spots using laser excitation at 514 nm wavelength. The Raman spectra in the dry condition is shown in Figure 46. No significant peak of nicotine was observed. From Figure 46, there is no enhancement from the three spots. All the three spots show similar low counts of intensity. For example, at wavenumber of 702 cm^{-1}, the intensity counts are 200, 230, and 300 for spot1, spot2, and spot3 respectively. This shows that there are some variation in intensity at different spots. The nanoparticles are so dispersed that the effects on the enhancement on Raman signal was not significant. In Figure 46, several peaks of

Raman signals are seen around the wavenumbers of 263, 412, 636, 702, and 907 cm^{-1}. In order to investigate the sources of peaks at these wavenumbers Raman spectra was collected from a dry mica sample which is shown in Figure 47. Similar peaks are found around the wavenumbers of 263, 412, 636, 702, and 907 cm^{-1}. That means the dry Raman spectra from dna_1 sample, shown in Figure 46, is from the mica substrate.

The Raman spectra of dna_1 sample at 1 ppt nicotine solution is shown in Figure 48. From Figure 48, it is seen that the intensity count varies in the range of 100 to 160 counts among the three spots at wavenumber 1030 cm^{-1} at which the characteristic nicotine peak is expected. The signal band around wavenumber 1030 cm^{-1} is also wide in all the spots spreading over from 1000 cm^{-1} to 1250 cm^{-1}. Since the intensity count is very low and the characteristic nicotine signal is spread over a wide range of wavenumbers, the Raman spectra from dna_1 sample are not considered successful SERS signals. The nanoparticles are so dispersed that the effects on the enhancement on Raman signal was not significant.

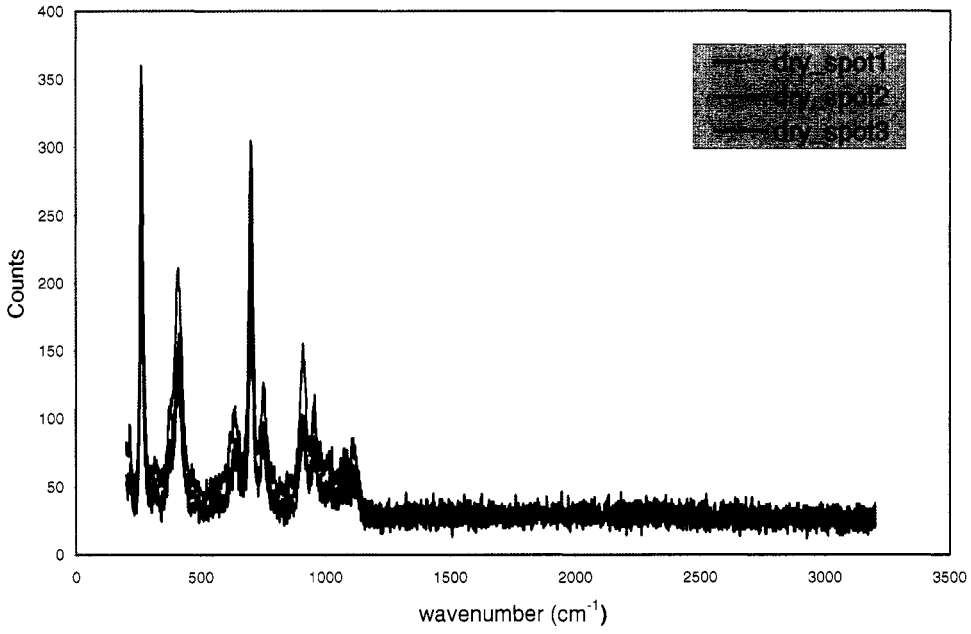

Figure 46. Raman spectra of the dna_1 sample at dry background.

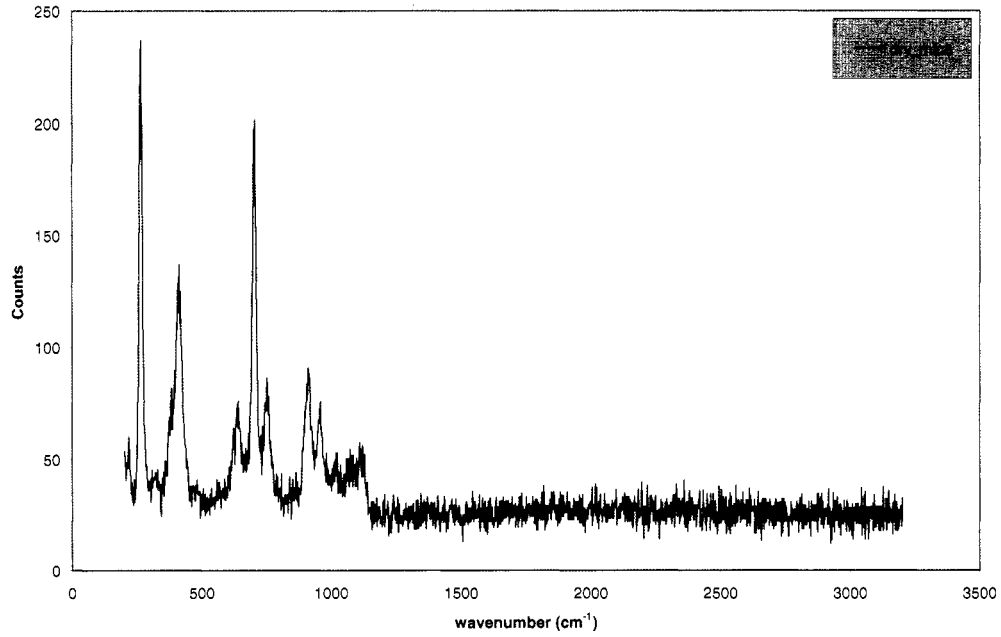

Figure 47. Raman spectra of the dry mica sample.

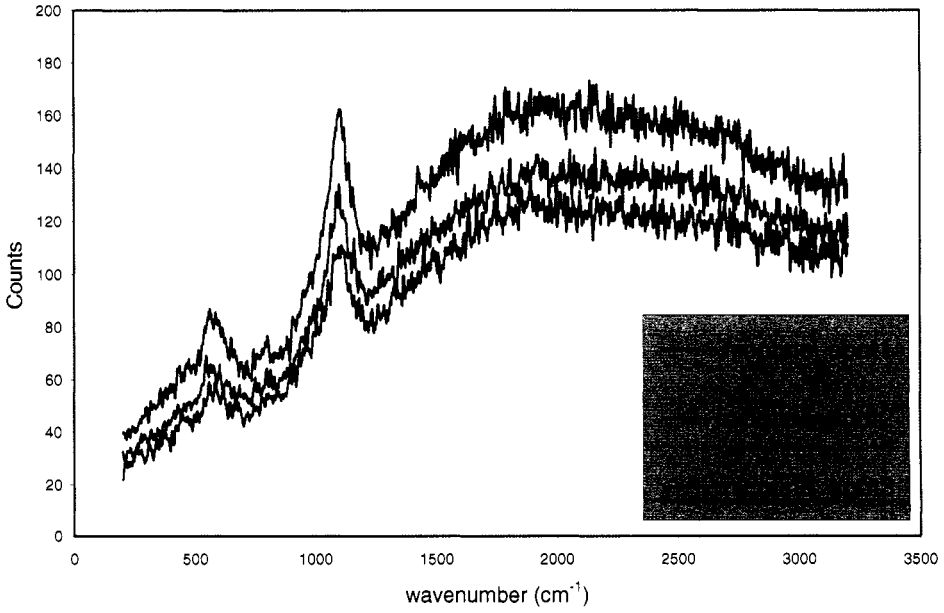

Figure 48. SERS spectra of dna_1 sample.

Samples dna_2 and dna_3 showed the same kind of spectra as dna_1 with nicotine. Raman spectra dry and with 1 ppt nicotine solution are shown in Figure 49 and Figure 50 respectively for dna_4 sample. In Figure 50, the peak around 1030 cm^{-1} represents the real nicotine peak of ring-breathing mode. The intensity of the nicotine peak is very low. Spectra were collected at four different spots. The mean intensity of nicotine peak is 4000 counts with relative standard deviation 25%. The spectra were recorded on Renishaw InVia Raman microscope with 514.5 nm excitation, 2.54 mW laser power, and 10 second exposure time.

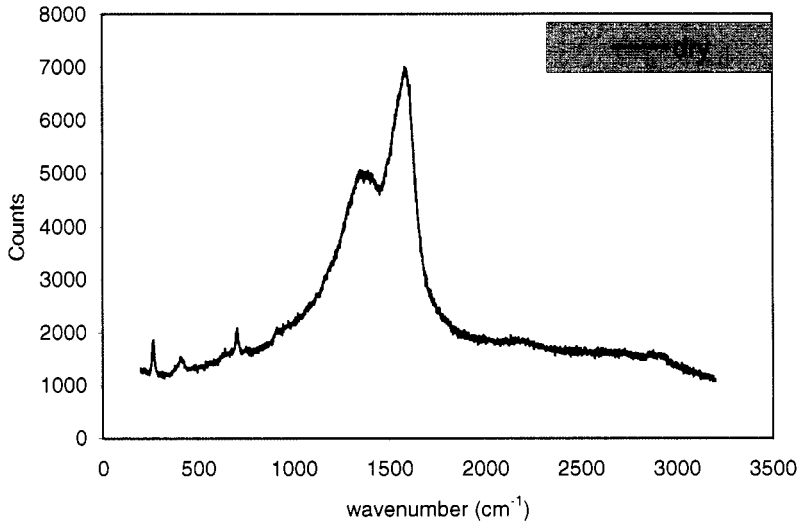

Figure 49. Raman spectra of dna_4 sample at dry condition.

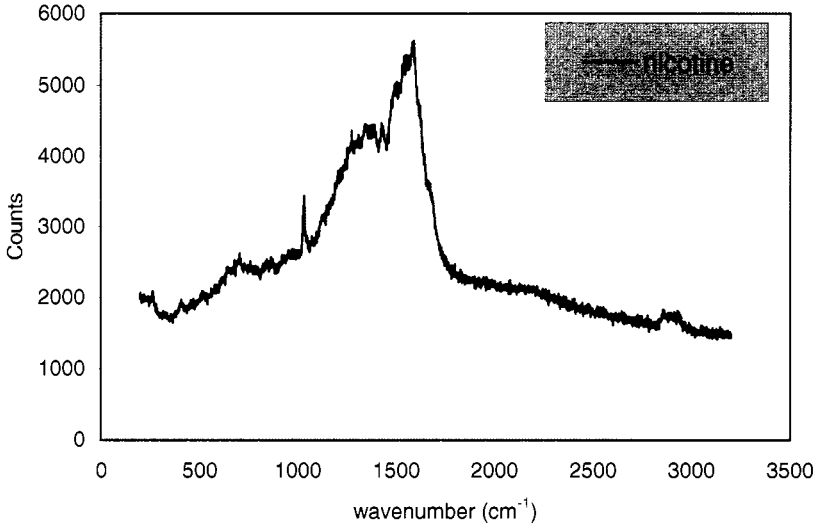

Figure 50. Raman spectra of dna_4 sample with 1 ppt nicotine.

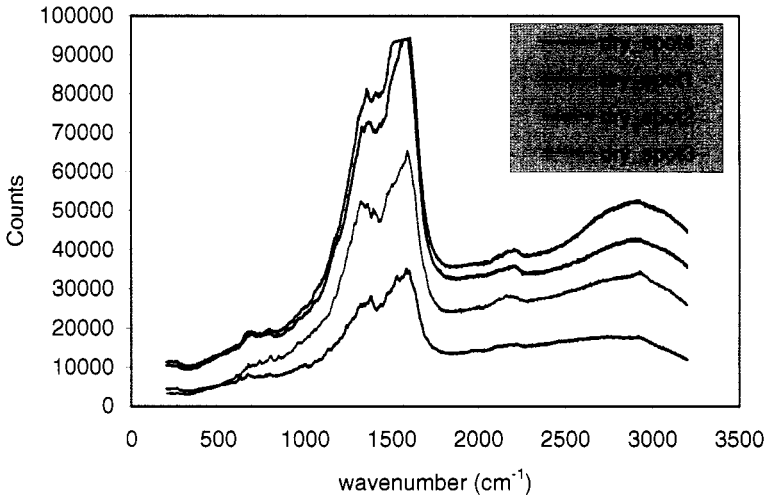

Figure 51. Raman spectra of dna_5 sample at dry condition.

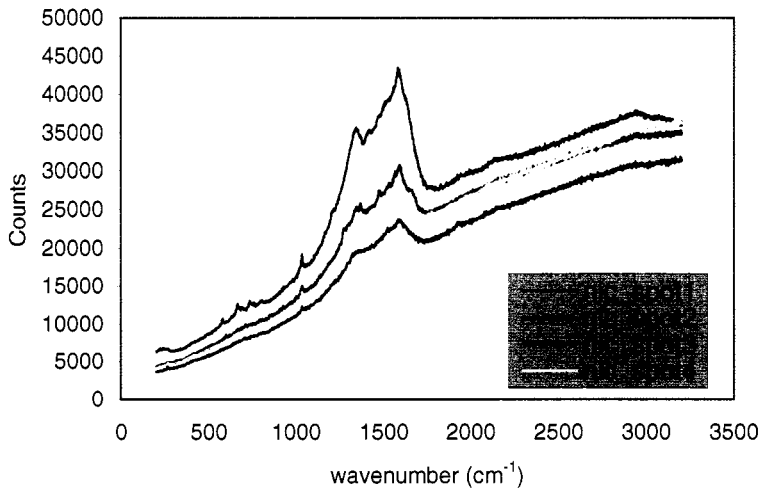

Figure 52. SERS spectra of dna_5 sample with 1 ppt nicotine solution.

The intensity of band at 1030 cm^{-1} enhanced 6 fold when the dna concentration is 148 ng/μl (Figure 52) compared with the Raman intensity formed when the dna concentration is 50 ng/μl (Figure 48).

To evaluate the uniformity of the sample, 121 spectra were taken at 220 μm by 220 μm area on dna_5 sample. The magnitude of the 1030 cm^{-1} Raman peak of nicotine are shown in Figure 53, where the dark square and white square represent 24000 and 62000 counts nicotine peak respectively. It may be noted that in the case of the highest nicotine signal, there is also a high background due to a large signal from the DNA.

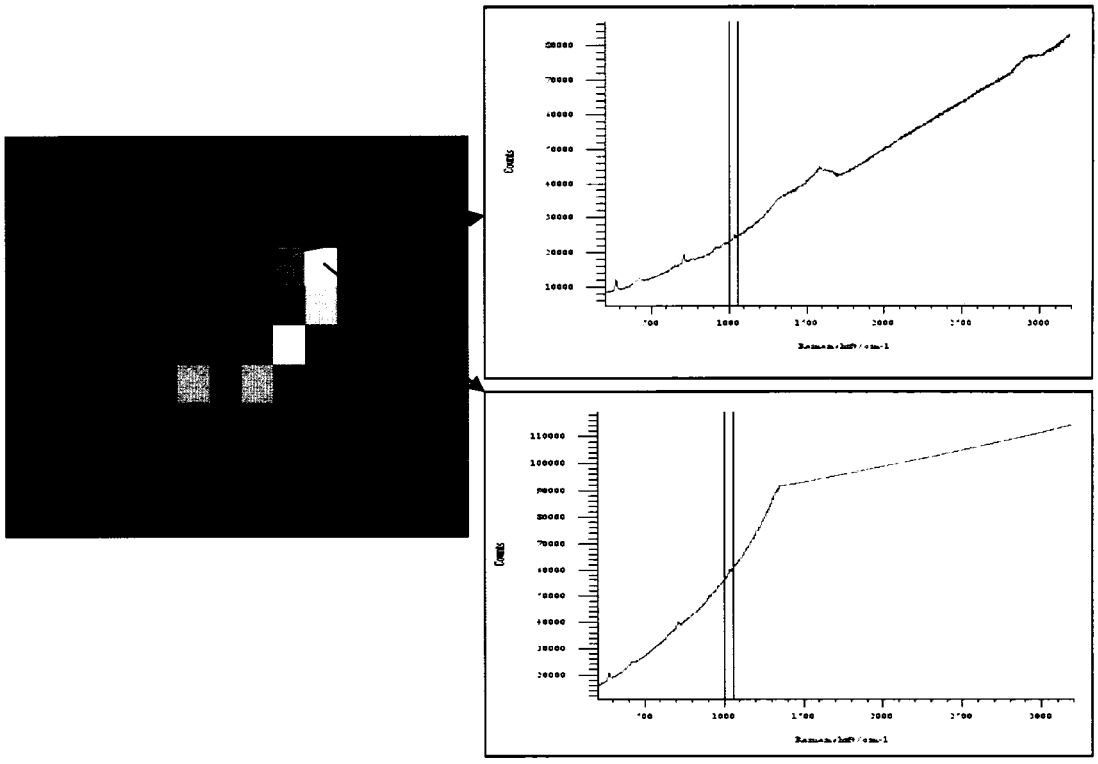

Figure 53. Mapping data of SERS spectra of dna_5 sample.

The average signal level is 16000 counts. Relative standard deviation observed is as 21.54 %. High standard deviation of the nicotine peak signal represents the non uniformity of the sample. As expected the solution chemistry based method can not ensure high reproducibility of the sample.

The dna_5 sample showed maximum enhancement compared to the others. The intensity of the nicotine peak is comparable to that with a sample prepared with standard method, electron beam lithography (EBL) which is shown in Figure 54. The SERS spectra were measured with laser at 488 nm. The laser power for these two

measurements was fixed at 3.73 mW. The high intensity background is due to the presence of DNA network.

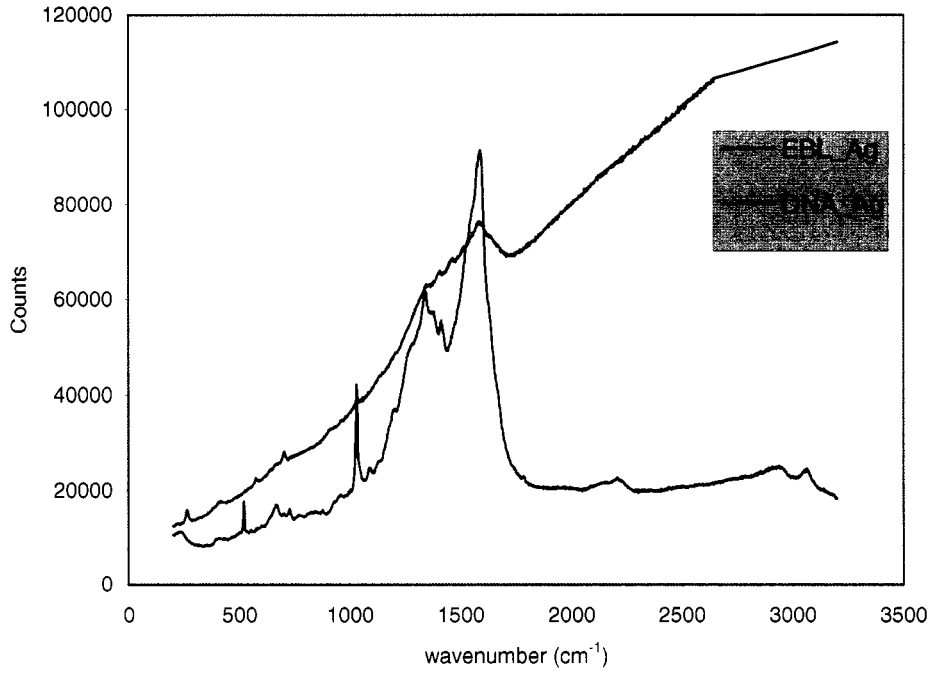

Fgure 54. Comparison of Raman spectra between the silver particles derived from the DNA and EBL.

Two schemes were done for DNA removal. Another sample was prepared following all the processing parameters as those of dna_5 sample. The sample is named dna_6. The sample was cut into two pieces. One piece of dna_6 sample was UV/ozonated for eight hours and then reduced in sodium borohydride solution for ten minutes. The SERS spectra with 1 ppt nicotine solution of the sample before and after

the treatment are shown in Figure 55. The presence of high background peak before and after the treatment indicates that the DNA has not been removed.

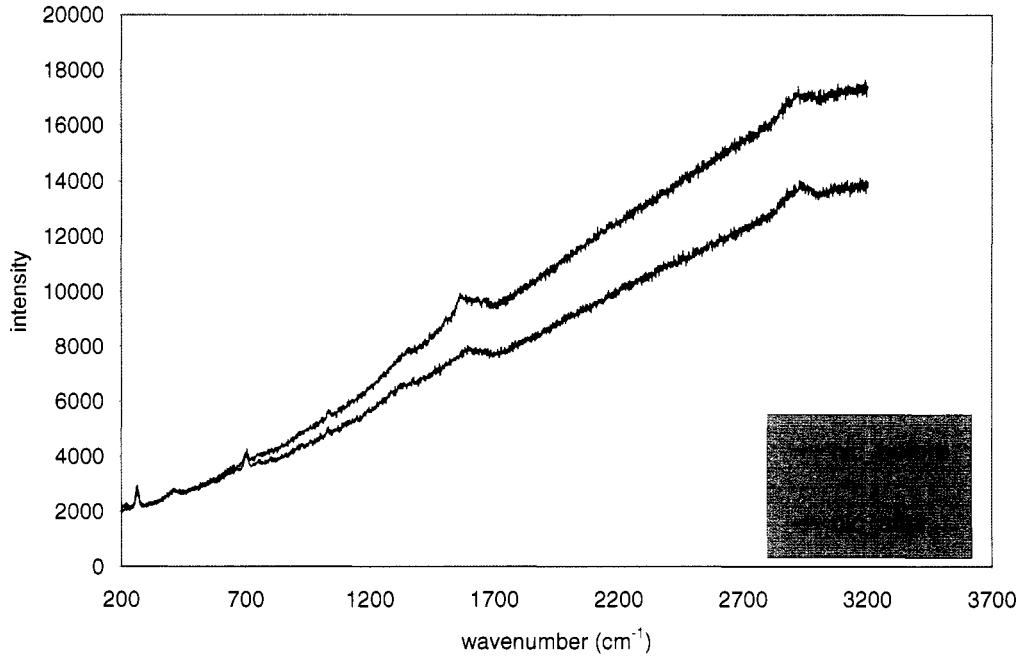

Figure 55. SERS spectra before and after treatment with UV ozone of dna_6 sample.

The other piece of dna_6 sample was treated with oxygen plasma for one hour and then reduced by sodium borohydride solution for 10 minutes. The SERS spectra before and after the treatment are shown in Figure 56. After the oxygen plasma treatment, the high background peak lowered. That means the DNA network was removed.

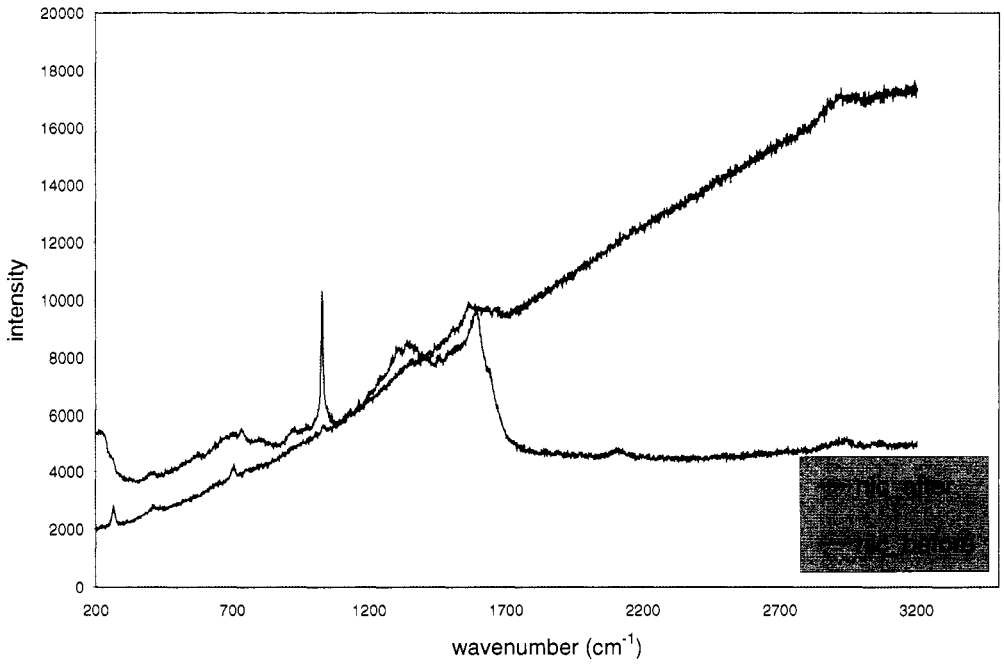

Figure 56. SERS spectra before and after DNA removal by using oxygen plasma.

After dna removal, 20 spectra were taken at 20 μm intervals over a 100 μm x 80 μm area on the dna_6 sample with 1 ppt nicotine solution. The average signal level for the 1030 cm^{-1} Raman peak of nicotine is 40679.22 counts. The observed relative standard deviation is 17%. This proves that highly enhancing SERS substrates can be prepared using DNA templating technique. While the uniformity of the sample is not as good as commercial substrates with < 10% standard deviation, it is possible that further improvements in the DNA deposition process could create further improvements in the uniformity of the silver nanoparticles.

5.3 Analysis on Silver Coated Silica Nanosphere

5.3.1 Morphological Analysis

Samples with silver coated silica nanosphere were prepared on glass substrates. A spin coater was used to deposit the silica beads on glass. 75 nm silver film was deposited on silica nanospheres. An SEM (model Hitachi S-570) was used to study the morphology of the samples at different spin speeds. SEM images showing the silica beads at the edge and near center of a sample prepared at 500 rpm spin speed are shown in Figure 57 and 58 respectively. The silica nanospheres are closely packed across the sample. However, for the sample prepared at 2000 rpm spin speed bead configuration at the center and near the edge shown in Figure 59 and 60 respectively are different. At the edge the silica beads are more closely packed whereas at the center they are sparcely distributed. An SEM image of a sample prepared at 3000 rpm spin speed shows nanospheres deposited at the center in Figure 61. At the higher speed, beads did not get time to be deposited uniformly all over the sample surface.

Figure 57. SEM image showing the silica nanosphere at the edge of the sample prepared at 500 rpm.

Figure 58 SEM image showing the silica nanosphere at near center of the sample prepared at 500 rpm.

Figure 59. SEM image showing the silica nanosphere at the edge of the sample prepared at 2k rpm.

Figure 60. SEM image showing the silica nanosphere near center of the sample prepared at 2k rpm.

Figure 61. SEM image showing the silica nanosphere at the center of the sample prepared at 3k rpm.

5.3.2 Characterization for SERS

Raman spectra of nicotine, deionized water, and ultra pure water were obtained from the silica nanosphere samples. A Raman spectrometer equipped with a 488 nm argon ion laser and liquid nitrogen cooled CCD detector was used for this analysis. The SERS characteristics of silver coated silica nanosphere samples were examined and compared with that from a silver coated plain glass sample. The Raman spectra of the samples from a dry condition were collected for background signal. The results of this control experiment presented in this section are labeled as dry.

In order to compare and measure the enhancement in Raman signals from the silver coated silica nanosphere samples, Raman spectra was obtained from the glass slide covered with 175 nm silver. Since there is no surface roughness on the sample, no enhancement due to surface plasmon resonance is expected. SERS spectra of Figure 62 was obtained by placing 1 ppt nicotine solution on a silver covered plain glass slide. A

corresponding dry experiment was done for a background signal. Figure 62 shows that the plain glass sample has no SERS characteristics.

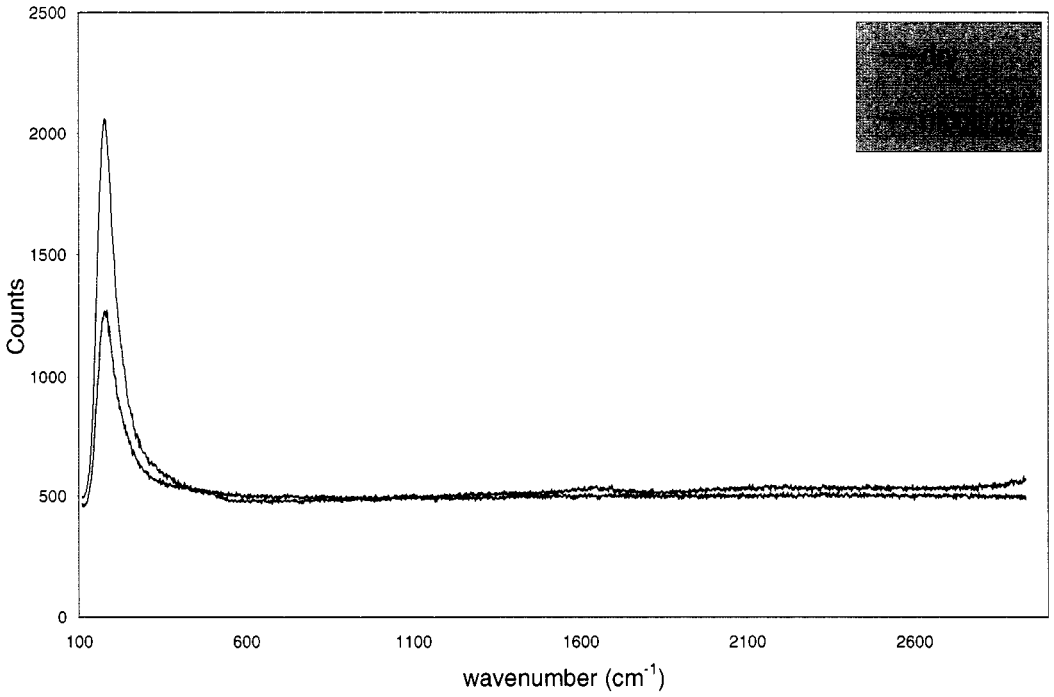

Figure 62. Raman spectra of glass covered with 175 nm Ag.

One drop of 1 ppt nicotine solution was placed in between the 50x objective and the silica nanosphere sample. Spots were chosen both at the center and the edge. The Raman spectra shown in Figure 63 and Figure 64 are for 4000 rpm and 3500 rpm samples respectively. The peak around 1050 cm^{-1} corresponds to the real nicotine peak. Raman spectra were also measured for dry samples and with deionized water. Both the samples had shown no enhancement at dry or from deionized water. Thus the peak around 1050

cm^{-1} from nicotine solution is undoubtedly due to nicotine in nicotine solution. Contamination peaks around 1500 to 2000 cm^{-1} appeared in every SERS signal.

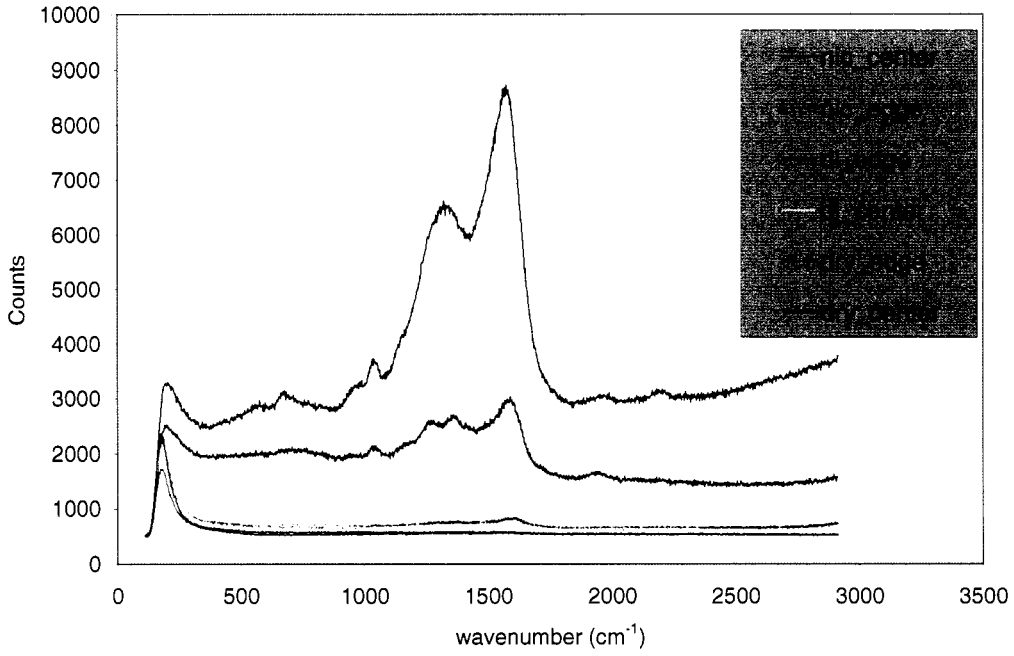

Figure 63. Raman spectra of 4000 rpm sample.

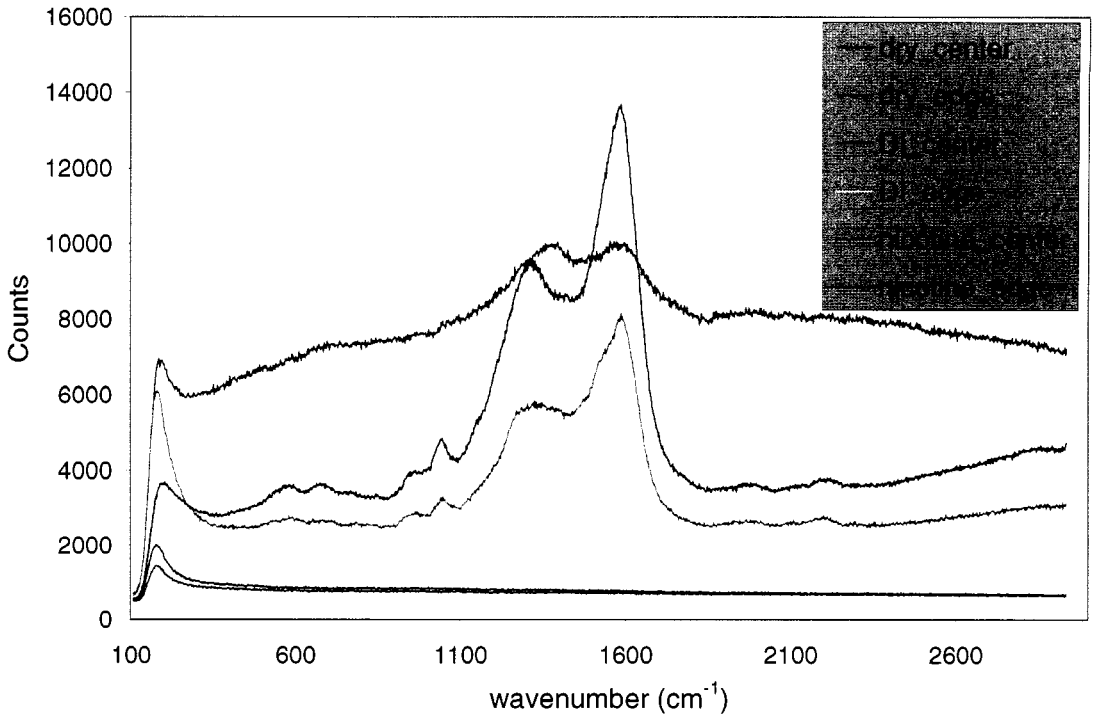

Figure 64. Raman spectra of 3500 rpm sample.

There is an inconsistency in intensity of the obtained spectra for dry and with liquid. This is due to the inefficiency of the objective of the Raman microscope to collect the scattered light from the wet sample. The microscope objective is not designed to work with liquid. The collection efficiency of light with the dry sample is not the same as with liquid. Also, intensity varies from spot to spot, because of the irreproducibility of the glass beads in the sample. There is also human error involved using the same spot as dry state and with solution.

Contamination peaks at around 1500 to 2000 cm^{-1} did appear consistently in all SERS spectra. Some sources for organic contamination might be deionized water, glass substrate, and silver. Three separate experiments were done to identify the sources of organic contamination. First investigation was done to see if the contamination was from the deionized water used to prepare the nicotine solution. Low organic pure water was purchased to replace the deionized water. Raman signals were measured for nicotine with ultrapure water. Figure 65 shows the Raman spectra measured for nicotine solution with ultrapure water. This spectra still showed the contamination peak, indicating the deionized water is not the source of this contamination.

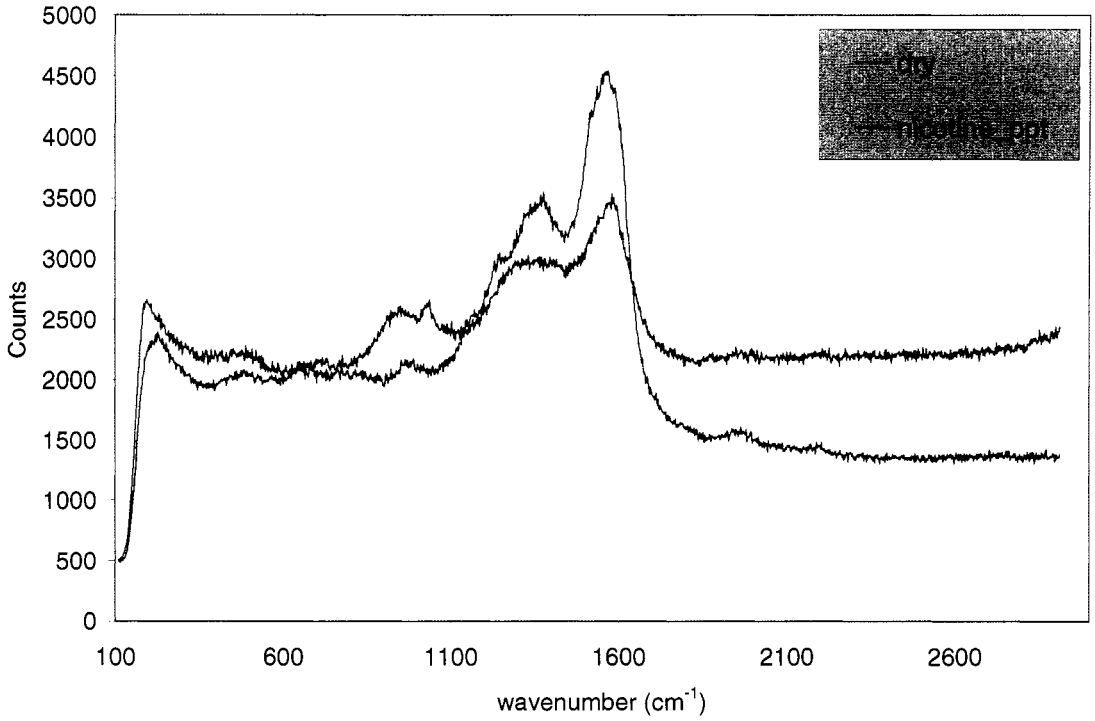

Figure 65. SERS spectra of 3k sample with nicotine solution prepared with ultrapure water.

Another experiment was done to find out if there is any relation to the contamination peaks with specific sample preparation methods. Raman data were taken for samples prepared by EBL to compare the Raman data with the Ag coated silica nanosphere samples. Raman spectra of the EBL sample for the dry state is shown in Figure 66. The Raman data from the EBL sample also shows the contamination peaks in the spectra. This comparison fairly concludes that there is no sample specific reason for the contamination peaks to appear in the specific wavenumbers.

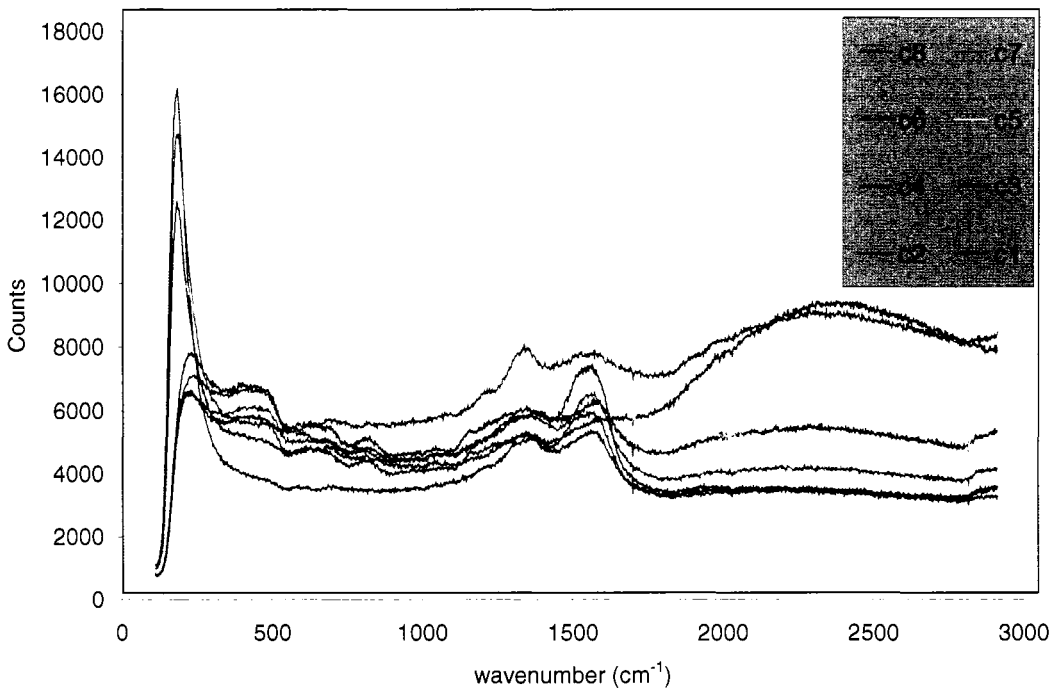

Figure 66. EBL sample in the dry state.

A third experiment was done to identify any effect of substrate type on the Raman spectra. Glass was used as substrate for the silica bead deposition in general. To compare with glass, a silicon substrate was used as the substrate. Silica nanosphere was deposited using a 4000 rpm spin speed. 40 nm silver was deposited using an E-beam evaporator. Raman spectra obtained from this sample for 1 ppt nicotine solution is shown in Figure 67. The intensity of the Raman spectra varies across the sample. The intensity is higher at some spots which are called hot spot. It can be seen from Figure 67 that the contamination peaks are present in the Raman spectra. Thus the results from this

experiment show that there is no relation to the substrate of the sample with this contamination peak.

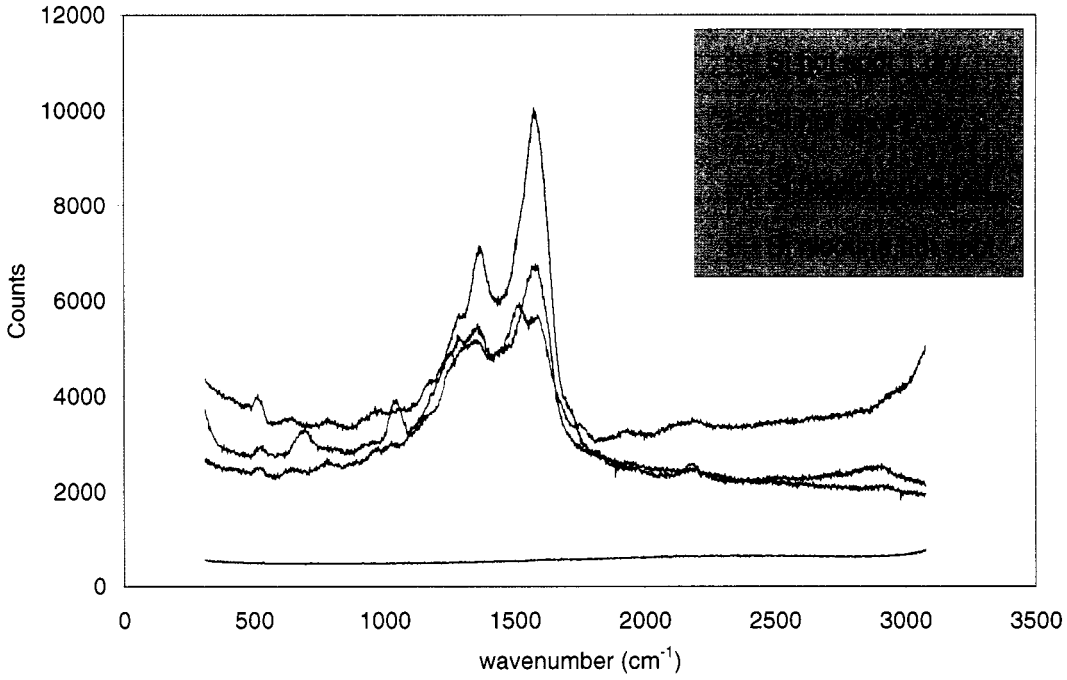

Figure 67. Raman spectra of Ag coated silica nanosphere on silicon sample.

The source of the contamination peaks at around 1500 to 2000 cm^{-1} was not identified. Whenever it is observed that means that spot is enhancing the Raman signal. The enhancement of the Raman signal comes from unknown sources.

CHAPTER 6

CONCLUSIONS AND FUTURE WORK

Silver nanoislands on silicon covered with thermal oxide were prepared using PS-PFEMS as a template. PS-PFEMS was used to control the size and shape of the nanoparticles. It was observed that the particle size and inter particle spacing were random. Inhomogenous diblock copolymer template is the primary reason of non periodic spacing and randomness of size of the silver particles in the sample in addition to the nonconformal silver film deposited at less than 10 nm thickness. The process of PS-PFEMS film deposition needs to be optimized further in order to obtain an array of silver particles with particular particle size and inter-particle spacing. Since spin speed and volume fraction of polymer in solution are critical in obtaining the cylindrical domains of PFEMS in PS matrix, more experiments need to be done to obtain an empirical relation of these variables with the two most important requirements of the template, pore size and spacing between them. This data will help to obtain polymer films with desired periodicity of PFEMS domains in PS matrix.

Wet etching was used to etch the PFEMS cylindrical domains. The effect of wet etching on the PS part was not studied. By comparing the SEM images of a sample before and after the etch the effect of etching on PS can be studied. SEM image of etched samples will also provide data on the pore size and spacing between the pores. However, SEM analysis of the polymer film could not be done in this work because of

the insulating nature of the polymer. SEM images of similar polymer film are reported in recent research [23].

Incomplete lift-off process can also affect the size and shape of the nanoparticles. The success of the lift-off process depends on the thickness of the polymer film. So to know the polymer film thickness is advantageous to optimize the polymer deposition and lift-off process. In order to use ellipsometry the refractive index data of the polymer must be known. Due to unavailability of refractive index data, the film thickness could not be determined. To get the thickness information SEM measurements on cross-sections is required. Due to the soft material, cross-sectioning was not possible.

Since PS-PFEMS is not commercially available, the etching chemistry was unknown. It was difficult to find selective etchant for the PFEMS. The concern related to the hazardous byproduct limits the options of using of etchants. For further study PS-PMMA can be used as a template. Since it is a commercially available material, all the necessary data can be found easily. The etching chemistry is also known.

Nanoparticles were also synthesized on mica substrate using λ-DNA as a template. This solution chemistry based method is simple and easy to apply. The particle size and shape can be controlled by choosing reducing time, the concentration of the reducing agent, and the concentration of the DNA solution. The effectiveness of the substrate was determined using nicotine solution as an analyte. It is observed that the enhancement is comparable to a standard EBL prepared SERS sample. Uniformity of the

sample is approximately two times poorer than the commercially available substrates prepared by Electron Beam Lithography [28].

The enhancement on Raman signal can be optimized by knowing the surface plasmon resonance wavelength of the particles. The surface plasmon resonance wavelength can be determined by UV-vis transmission measurement. However, this can only be done for transparent substrates. Since mica is opaque to white light, UV-vis measurements could not be done to get the surface plasmon resonance wavelength data. Further study can be done by using glass as a substrate. Since glass is transparent, it would be possible to do the UV-vis measurement. In addition to that, the hydrophilicity of the glass could offer the flexibility to apply all the steps that were used on mica.

Thin film covered silica nanosphere samples were prepared to study the SERS effect using different analytes such as nicotine solution, benzoic acid, and 1-octadecanethiol. Although characteristic Raman peak was observed for nicotine, no characteristic Raman peak was observed for other analytes such as benzoic acid and 1-octadecanethioL. Silver quickly oxidizes and forms silver oxide film on the silica nanospheres of the samples. Experiments to measure Raman signals using nicotine were done before doing the measurements for other analytes. There is a possibility that a silver oxide film between the analytes and the silver coated nanospheres were present during the measurement because of oxidation of the samples. This silver oxide layer can change and limit the resonance properties of the sample which might result in little or no enhancement of Raman signals. In order to avoid this, experiments need to be done using

freshly prepared samples for all types of analytes. Samples prepared with gold covered nanospheres can be used repeatedly since gold is stable in air.

Contamination peaks in Raman spectra were consistently observed for all analytes. Investigative experiments were done to identify the sources of the contamination peaks. While all probable sources associated with sample preparation and experimental setup were investigated, elemental analysis of samples using XPS or AES can be done to further study the source of contamination.

REFERENCES

1. B. Schrader, Infrared and Raman Spectroscopy Methods and Applications, 3rd ed. (Weinheim Univ. Press. Weinheim, Germany, 1995), pp. 489-491.

2. K.Kneipp, H. Kneipp, I. Itzkan, R.R. Dasari and M.S. Feld, "*Surface-enhanced Raman scattering and biophysics*," Journal of Physics: Condensed Matter, **14**, 597-624 (2002).

3. S. Nie and S.R. Emory, "*Probing Single Molecules and Single Nanoparticles by Surface-Enhanced Raman Scattering*," Science, **275,** 1102-1106 (1997).

4. M. Moskovits, *"Surface-enhanced spectroscopy,"* Rev. Modern Physics, **57**, 783-821 (1985).

5. T. Thurn-Albrecht, R. Steiner, J. DeRouchey and C.M. Stafford, *"Nanoscopic Template from Oriented Block Copolymer Films*," Advanced Materials, **12**, 787-791 (2002).

6. G. Wei, H. Zhou, Z. Liu and Y. Song, *"One-step Synthesis of Silver Nanaparticles, Nanorods, and Nanowires on the Surface of DNA network,"* J.Phy. Chem. B, **109**, 8738-8743 (2005).

7. D.Y.Wu, B.Ren and Z.Q. Tian, "*Progress in the Theory of Surface Enhanced Raman Scattering,*" The International Journal of Vibrational Spectroscopy, **4**, 2-38 (2005).

8. C.J. Hicks, "*Surface Enhanced Raman Spectroscopy*," unpublished results.

9. G. Cardini, M. Muniz-Miranda and V. Schettino, *"SERS and DFT Study on 4-Methylpyridine Adsorbed on Silver Colloids and Electrodes,"* J. Physical Chemistry B, **108**, 17007-17011 (2004).

10. J.G. Grasselli and B.J. Bulkin, Analytical Raman Spectroscopy, 1st ed. (John Willey & Sons, Inc, 1991) pp. 93-100.

11. T.Vo-Dinh, "Surface-enhanced Raman Spectroscopy using metallic nanostructures," Trends in Analytical Chemistry, 17, 557-581 (1998).

12. C. Park, J. Yoon and E.L. Thomas, *"Enabling nanotechnology with self-assembled block copolymer patterns,"* Polymer, **44,** 6725-6760 (2003).

13. N.C. Seeman, *"DNA in a material world,"* Nature, **42**, 427-430 (2003).

14. R.L. Moody, T. Vo-Dinh and W.H. Fletcher, *"Investigation of Experimental Parameters for Surface-Enhanced Raman Scattering (SERS) Using Silver-Coated Microsphere Substrates,"* Applied Spectroscopy, **41**, 966-970 (1987).

15. L.L. Bao, S.M. Mahurin, C. Liang and S. Dai, *"Study of silver films over silica beads as a surface-enhanced Raman scattering (SERS) substrate for detection of benzoic acid,"* Journal of Raman Spectroscopy, **34**, 394-398 (2003).

16. C.L.Haynes and R.P.V.Duyne, *"Nanosphere lithography: a versatile nanofabrication tool for studies of size-dependent nanoparticle optics,"* J. Phys. Chem, **105**, 5599-5611 (2001).

17. J.C.Hulteen, D.A.Treichel, M.T.Smith, M.L.Duval, T.R.Jensen and R.P.V.Duyne, *"Nanosphere lithography: size-tunable silver nanoparticle and surface cluster arrays,"* J. Phys. Chem, **103**, 3854-3863 (1999).

18. A.D.Ormonde, E.C.M.Hicks, J.Castillo and R.P.V.Duyne, *" Nanosphere lithography: fabrication of large-area Ag nanoparticle arrays by convective self-assembly and their characterization by scanning UV-visible extinction spectroscopy,"* Langmuir, **20**, 6927-6931 (2004).

19. C.L.Haynes and R.P.V.Duyne, *"Plasmon-Sampled Surface-Enhanced Raman Excitation Spectroscopy,"* J. Phys. Chem, **107**, 7426-7433 (2003).

20. T. R. Jensen, M.D.Malinsky, C.L.Haynes and R.P.V.Duyne, *"Nanosphere lithography: tunable localized surface plasmon resonance spectra of silver nanoparticles,"* J. Phys. Chem, **104**, 10549-10556 (2000).

21. J.B. Jackson, S.L. Westcott, L.R. Hirsch and N.J. Halas, *"Controlling the surface enhanced Raman effect via the nanoshell geometry,"* App Physics Letters, **82**, 257-259 (2003).

22. J.B. Jackson and N.J. Halas, *"Silver Nanoshells: Variations in Morphologies and Optical Properties,"* American Chemical Society, **105**, 2743-2746 (2001).

23. K.W. Guarini, C.T. Black and S.H.I. Yeung, *"Optimization of Diblock Copolymer Thin Film Self Assembly,"* Advanced Materials, **14,** 1290-1294 (2002).

24. T.M. Rana and C.F. Meares, *"Specific cleavage of a protein by an attached Iron Chelate,"* J. Am. Chem. Soc. **112**, pp 2457-2458 (1990).

25. J. Lu, Agilent Technologies Laboratories, *private communication (January 2005).*

26. W.A. Zisman, *"Relation of equilibrium contact angle to liquid and solid constitution,"* ACS Adv. Chem. Ser, **43**, 1-51 (1961).

27. T.E. Barber, M.S. List, J.W. Haas and E.A. Wachter, *"Determination of nicotine by Surface Enhanced Raman Scattering (SERS),"* Applied Spectroscopy, **48**, 1423-1427 (1994).

28. JOHN, L., 2005. *Klarite substrates for surface enhanced Raman spectroscopy-new product release* [Online]. Available at http://www.mesophotonics.com (accessed 10 July 2005).